Check for updates

Halide perovskite quantum dots for photocatalytic CO$_2$ reduction

Wentao Song, Guobin Qi and Bin Liu [ID] *

Halide perovskite quantum dots have recently attracted increasing research interest in photocatalytic CO$_2$ reduction due to their high light absorption coefficient, tunable bandgap, and long charge diffusion length. However, the intrinsic high radiative recombination and instability of perovskite quantum dots limit the development of perovskite-based photocatalysis, which is under investigation by different research groups. This review is focused on the current progress and challenges of halide perovskite quantum dots for photocatalytic CO$_2$ reduction. The structures and properties of perovskite quantum dots as well as the mechanism and obstacles for photocatalytic CO$_2$ reduction are first summarized in detail. Subsequently, composition optimization, surface modification, and heterojunction construction of perovskite-based photocatalysts are introduced to enhance photogenerated carrier separation and photocatalytic CO$_2$ activity. Finally, we discuss the challenges and opportunities of perovskite quantum dots for photocatalytic CO$_2$ reduction and further propose several prospective directions for future research.

10th anniversary statement

Since the *Journal of Materials Chemistry* was split into three independent journals (*A*, *B*, and *C*) in 2013, the *Journal of Materials Chemistry A* has developed rapidly into one of the leading scientific journals in the energy and sustainability fields. Over the past 15 years, our group and co-workers have published 16 papers in the *Journal of Materials Chemistry* (*A*, *B*, and *C*), which include various topics, such as dye-sensitized solar cells, perovskite solar cells, water splitting, and CO$_2$ reduction. With the strong support from the materials and energy community, we wish JMCA great success and hope that it will grow to be one of the most influential journals in the near future.

1. Introduction

Photocatalytic CO$_2$ reduction is one of the very effective and environmentally friendly strategies to convert CO$_2$ to valuable chemical fuels.[1,2] In pursuit of high CO$_2$ conversion efficiency, many semiconductor photocatalysts with appropriate energy bands have been utilized for photocatalytic CO$_2$ reduction.[3–5] Nonetheless, the solar-to-fuel efficiency is far lower than 10%, making it less suitable for large-scale industrial production. The high recombination rate and low efficiency of photocatalysts prevent their widespread applications.[6–8]

Since the pioneer work of halide perovskite materials in solar cells by Miyasaka in 2009,[9] halide perovskite materials have attracted much research interest in optoelectronics and photoelectrical conversion.[10,11] In 2015, Kovalenko and colleagues synthesized perovskite quantum dots (QDs) or nanocrystals (NCs) through the hot-injection method for the first time.[12] The relatively stable perovskite QDs have great potential for practical applications in various photoelectrical

Department of Chemical and Biomolecular Engineering, National University of Singapore, Singapore 117585, Singapore. E-mail: cheliub@nus.edu.sg

fields, including solar cells, light-emitting diodes (LEDs), photodetectors, and so on.[13–17] Recently, perovskite QDs have been explored for photocatalytic CO$_2$ reduction due to their high light absorption coefficient, tunable bandgap, and long carrier transport distance.[18,19] Photocatalysis generally involves several key processes: light absorption, photogenerated carrier separation and migration, surface catalytic reaction, and product desorption. The high light absorption coefficient means more light can be captured for photocatalytic CO$_2$ reduction. The tunable bandgap allows perovskite to easily optimize the bandgap and redox potential, and the long carrier diffusion distance shows great opportunity for carriers to migrate to the active site. These unique properties could make perovskite QDs promising photocatalysts for CO$_2$ reduction. However, the radiative recombination induced by high photoluminescence quantum yield (PLQY) and low stability against light, heat, oxygen, and moisture of perovskite QDs have an adverse effect on photocatalytic CO$_2$ reduction.[20,21] To overcome these obstacles, some methods have been developed to improve the photocatalytic CO$_2$ performance of perovskite QDs.[22] For example, various heterojunction composites were constructed to enhance the photogenerated carrier separation and photocatalytic stability

for highly efficient CO_2 reduction.[23] A series of composition optimization and surface modification measures have been performed to improve the stability and efficiency of perovskite-based photocatalysts. Although several reviews have summarized the current progress of different photocatalytic processes and stability issues, nevertheless, very few reports were focused on perovskite QDs for photocatalytic CO_2 reduction or discussed the difficulties of photocatalytic CO_2 reduction from the perspective of perovskite fundamentals and the photocatalytic mechanism.[24,25] In addition, despite the considerable progress made for CO_2 photoreduction, it is noteworthy that the superior photocatalytic activity and long-term stability of perovskite photocatalysts are yet to be realized.[26] It is thus important to understand the photocatalytic mechanism, summarize the current progress, and provide insightful

perspectives into further development of perovskite QDs for photocatalytic CO_2 reduction.[27,28]

This review highlights the recent success and reliable measures of perovskite-based photocatalysts for CO_2 photoreduction, and proposes appropriate strategies for future design, as shown in Fig. 1. First, the fundamentals of perovskite QDs, as well as the mechanism and obstacles for photocatalytic CO_2 reduction are summarized in detail. Afterwards, current successful strategies, including composition optimization, surface modification and heterojunction construction, are introduced to enhance the photocatalytic CO_2 activity and stability of perovskite-based photocatalysts. Finally, we discuss the challenges and opportunities of perovskite QDs for photocatalytic CO_2 reduction and further propose several prospective directions for future research.[29]
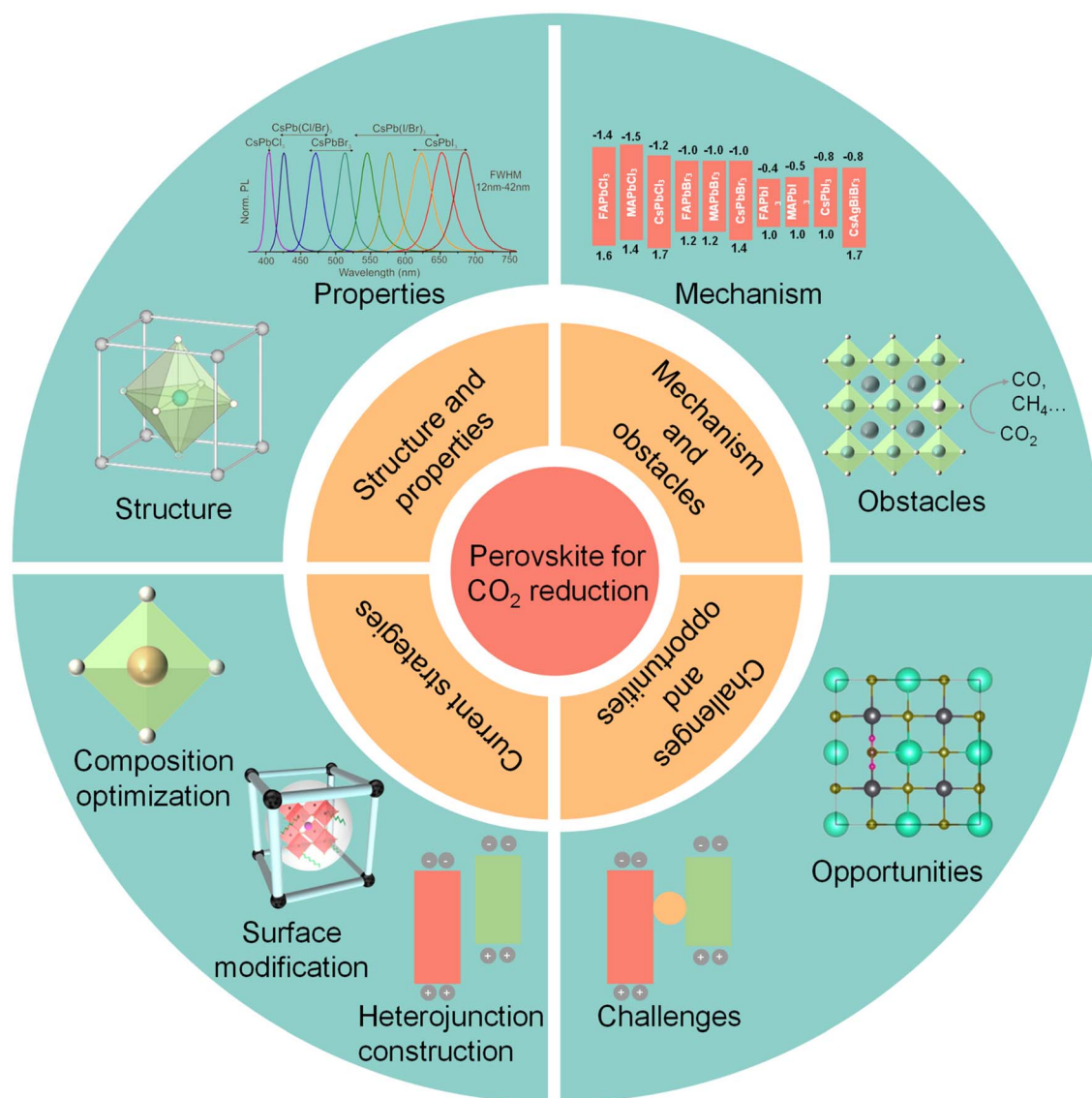
Fig. 1 Schematic illustrations of halide perovskite QDs for CO_2 reduction: structure and properties, photocatalytic mechanism and obstacles, current strategies, challenges, and opportunities. Reproduced from ref. 17 with permission from American Chemical Society, copyright 2015; reproduced from ref. 91 with permission from Wiley-VCH, copyright 2022; reproduced from ref. 105 with permission from Royal Society of Chemistry, copyright 2022.

This journal is © The Royal Society of Chemistry 2023

J. Mater. Chem. A, 2023, **11**, 12482–12498 | **12483**

2. Halide perovskite fundamentals, photocatalytic mechanism, and obstacles for CO_2 reduction

2.1 Crystal structure and properties

2.1.1 Crystal structure. The general chemical formula of halide perovskite is ABX_3 (A = Cs^+, $CH_3NH_2^+$ (MA^+), or $CH_2(NH_2)_2^+$ (FA^+), B = Pb^{2+}, or Sn^{2+}; X = Cl^-, Br^-, or I^-).[30] The B^{2+} cation coordinates with six X^- anions to form $[PbX_6]^{4-}$ octahedra, surrounded by eight A^+ cations, as shown in Fig. 2a.[31] According to element composition, the halide perovskite structure could be divided into organic–inorganic hybrid perovskites and all-inorganic perovskites. Based on the chemical formula and atom radius, Goldschmidt's tolerance factor ($t = \dfrac{r_A + r_X}{\sqrt{2}(r_B + r_X)}$, r_A, r_B, and r_X represent the radii of A, B, and X, respectively) is used to measure the structural stability of perovskite materials.[31] When t ranges from 0.8–1, it fits structural constraints and constructs stable three-dimensional perovskite. Nonetheless, when the radius of the A cation is too large, it would cause t to be larger than 1 and usually form lower-dimensional phases, such as two-dimensional (2D) perovskites (*e.g.*, A_2PbI_4), whereas when t is smaller than 0.8, other structures, such as perovskite oxide (ABO_3), are stable.[32]

In addition, according to the bond angle of Pb-X-Pb, the halide perovskite structure can be divided into optically active black perovskite phases: cubic (α), tetragonal (β), and orthorhombic (γ) phases. The ideal Pb-X-Pb angle is 180°, corresponding to cubic perovskite. The distortion of the cubic structure would change the angle of Pb-X-Pb and reduce the crystal symmetry, which would form low symmetric tetragonal and orthorhombic perovskite.[33] Fig. 2b depicts the crystal structure of different phases and their relative phase transitions of $CsPbI_3$. At room temperature, the metastable black perovskite phases would undergo phase transformation into the stable non-perovskite phase (δ-$CsPbI_3$), which is non-photoactive and undesirable for optoelectronics.

2.1.2 Band structure and optical properties. Up till now, perovskite QDs have been successfully utilized for optoelectronics due to unique optical properties, such as long carrier lifetime, and high absorption coefficient, and tunable bandgaps. Fig. 3a shows the composition of the conduction band (CB) and valence band (VB) of perovskite QDs ($CsPbX_3$). The antibonding hybrid state of 6s orbitals of Pb^{2+} and np orbitals of X^- (n = 3, 4, and 5 for Cl, Br, and I, respectively) mainly participate in the composition of the VB, while the CB consists of the antibonding hybrid state from 6p orbitals of Pb^{2+} and np orbitals of X^-. Both the CB and VB are dominated by the antibonding orbitals from B-site cations and X-site anions, leading to either shallow trap states or defects resonant within the CB or VB, which would not form a recombination centre within the bandgap.[34,35] For traditional semiconductors (such as CdSe and GaAs), the bandgaps are normally formed by the bonding orbitals (VB) and antibonding orbitals (CB), which are prone to form deep trap states within the bandgap. This high defect-tolerant property makes perovskite QDs display a much longer lifetime than traditional semiconductors, demonstrating great potential for photocatalysis.[36] Because B-site cations and X-site anions directly contribute to the construction of the CB and VB, while A-site cations do not participate in the composition of
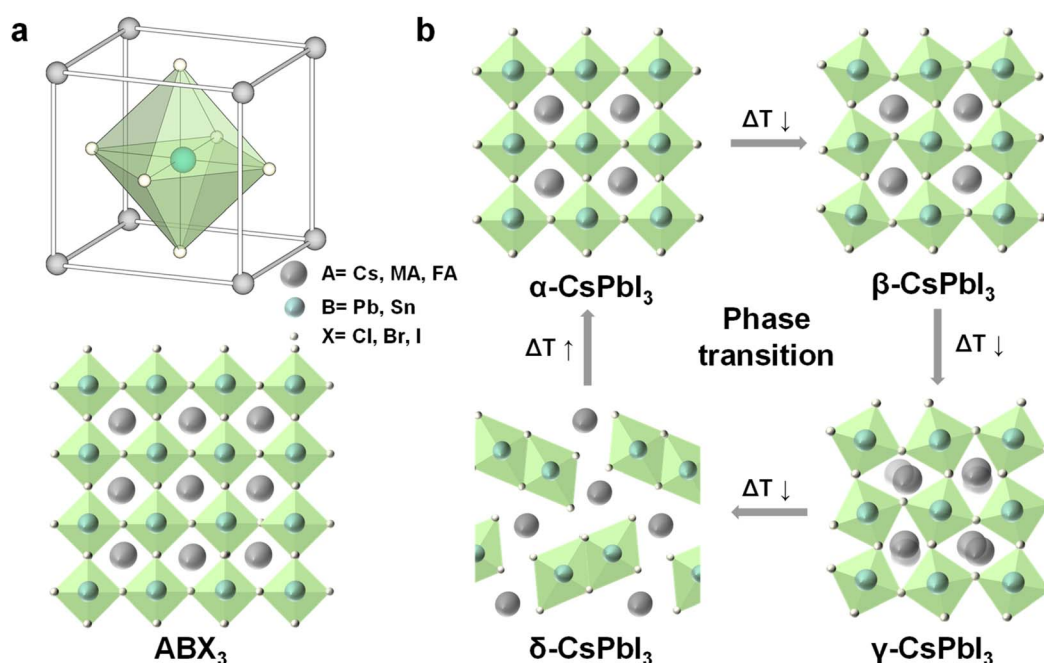
Fig. 2 (a) Illustration of the halide perovskite structure ABX_3, A = Cs^+, $CH_3NH_2^+$ (MA^+), or $CH_2(NH_2)_2^+$ (FA^+), B = Pb^{2+}, or Sn^{2+}; X = Cl^-, Br^-, or I^-; (b) crystal structure of the different $CsPbI_3$ phases and relative phase transitions. Reproduced from ref. 33 with permission from American Association for the Advancement of Science, copyright 2019.

12484 | *J. Mater. Chem. A*, 2023, **11**, 12482–12498

This journal is © The Royal Society of Chemistry 2023
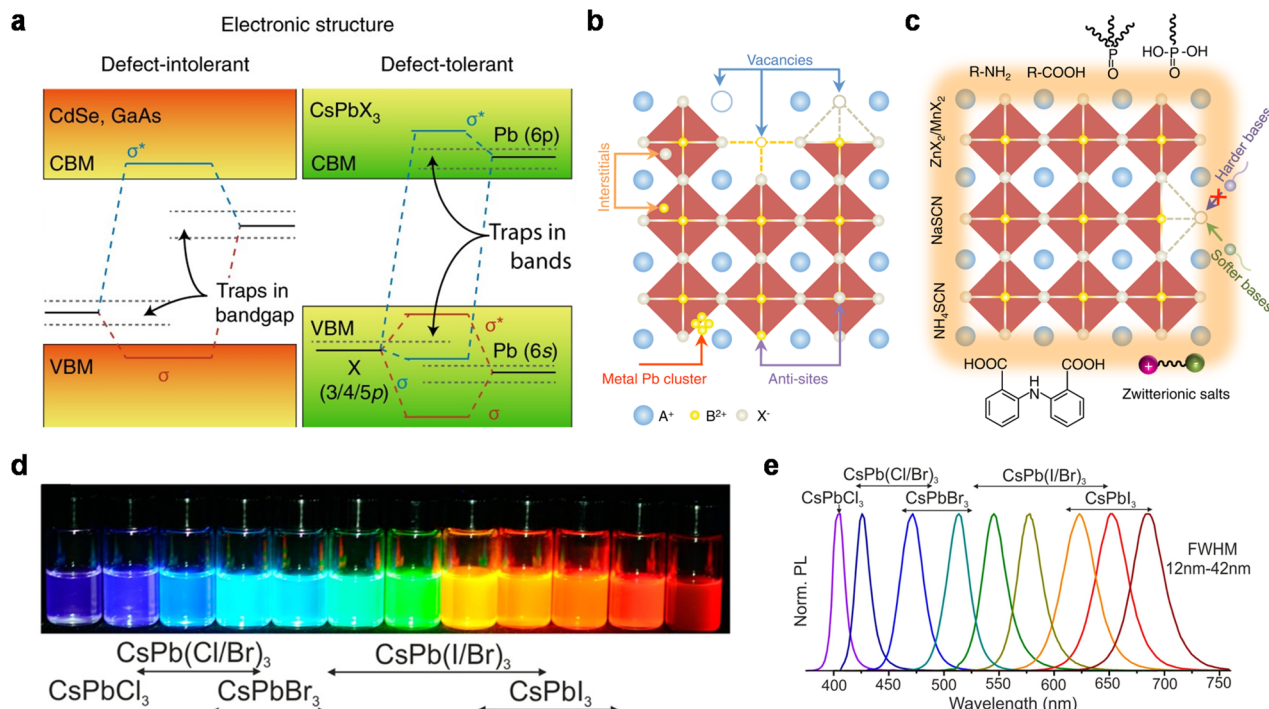
Fig. 3 (a) Scheme of the electronic band structure of typical defect-intolerant semiconductors and perovskite QDs. In conventional semi-conductors, the bandgap is formed between bonding (σ) and antibonding (σ^*) orbitals. Point defects or dangling bonds emerge as weak bonding or non-bonding states within the bandgap. In perovskite QDs, the bandgap is formed between two antibonding orbitals. Only shallow traps are formed within the CB or VB, with little influence on optical properties. Reproduced from ref. 35 with permission from Springer Nature, copyright 2018. (b) Point defects of perovskite QDs, including vacancies, interstitials, anti-sites, and metal Pb clusters. Reproduced from ref. 39 with permission from Springer Nature, copyright 2021. (c) Common passivating ligands for perovskite QDs: zwitterionic salts, R−NH$_2$, R−COOH, *etc.* Reproduced from ref. 39 with permission from Springer Nature, copyright 2021. (d) Perovskite QDs in toluene under a UV lamp ($\lambda = 365$ nm). Reproduced from ref. 17 with permission from American Chemical Society, copyright 2015. (e) Representative PL spectra of mixed-halide perovskite QDs. Reproduced from ref. 17 with permission from American Chemical Society, copyright 2015.

band-edge, the A-site cations were conventionally believed to hardly affect the optoelectronic properties of perovskite materials. Nonetheless, more and more reports indicate that A-site cations would also change the physicochemical and optoelectronic properties, including stabilities, bandgaps, and charge transfer, because different A-site cations could influence crystal symmetries, phase stabilization, and ion migration.[37] Besides, the labile native ligands, and low defect formation energy indicate that it is easy to generate trap states on the surface of perovskite. These trap states mainly involve point defects, including halide and A-site vacancies, anti-sites, and so on (Fig. 3b).[38] Many defect passivation strategies have been designed, one of which uses agents to neutralize the charged defects *via* extra coordination or ionic bonding. Lewis acid/base moieties and positively/negatively charged organic components are generally used to passivate these defects (Fig. 3c).[39] To understand these passivation agents, hard–soft acid–base theory has been developed.[40] For example, compared to oleyl-amine, softer bases (alkylphosphonates and sulfonates) can passivate defects effectively because of higher binding affinity, while harder bases can hardly reduce defects owing to a hard–soft mismatch between hard groups and soft Pb binding sites. Additionally, the molar extinction coefficient of perovskite QDs is about 10^5–10^7 L mol^{-1} cm^{-1}, an order of magnitude higher

than that of traditional semiconductors. In contrast to tradi-tional semiconductors, the higher molar extinction coefficient of perovskite QDs could allow them to absorb more light to excite photogenerated electrons and holes for efficient opto-electrical conversion. Furthermore, the efficient anion exchange of perovskite QDs can help realize full visible-light absorption, which indicates a simple strategy for bandgap tuning (Fig. 3d and e). The bandgap can be achieved from 1.6 to 3.0 eV in mixed halide perovskite by simply changing the ratio of Cl : Br or Br : I. The tunable bandgap makes perovskite QDs good candidates for efficient photocatalysts.

2.2 Photocatalytic mechanism

Photocatalysis refers to a chemical reaction with the aid of light and a photocatalyst, which can absorb light to promote electron excitation from the VB to the CB, and thus leave holes in the VB. The photogenerated electron and hole pairs can be used for two half-reactions: reduction and oxidation reactions. Taking CO_2 reduction by H_2O as an electron source as an example, the CB minimum of a photocatalyst must be more negative than the electrochemical potential of CO_2 reduction and the VB maximum must be more positive than the electrochemical potential of H_2O oxidation to ensure that the reaction can occur. That is to say, the bandgap of a photocatalyst should meet the

This journal is © The Royal Society of Chemistry 2023

J. Mater. Chem. A, 2023, **11**, 12482–12498 | **12485**

band requirement of both CO_2 reduction and H_2O oxidation, which limits the selection of a single photocatalyst. Therefore, sacrificial agents with lower oxidation potentials are added to replace H_2O and decrease the required bandgap.[41] Considering the photocatalytic thermodynamics, a proper energy band plays a vital role in reaction redox potentials. The redox potentials of perovskite QDs together with traditional semiconductors and photocatalytic CO_2 reduction to C_1 products are depicted in Fig. 4. It could be clearly seen that the CBs of perovskite QDs are more negative than that of traditional semiconductors, which means perovskite QDs are more favourable for CO_2 reduction and H_2 production. However, when it comes to water oxidation for O_2 production and $\cdot OH$ production, nearly all the perovskite QDs cannot perform this reaction owing to the weak oxidation potentials. Notably, most traditional semiconductors show good potential for O_2 production, indicating suitable candidates to form a heterojunction with halide perovskite QDs. From the standpoint of thermodynamics, halide perovskite QDs could yield all the C_1 products from photocatalytic CO_2 reduction. In fact, photocatalytic CO_2 reduction is strongly affected by both thermodynamics and kinetics.[42,43] For example, CO_2 reduction to CO or HCOOH involves a $2H^+/2e^-$ process, and this multiparticle (from bond breaking of the CO_2 molecule to bond formation of CO or HCOOH molecules) transfer faces kinetic limitations. For the $6H^+/6e^-$ processes of CO_2 reduction to CH_3OH, the complex multiparticle and multielectron processes are less favourable in a single photocatalytic reaction. Thus, despite all the C_1 products meeting thermodynamic conditions, the general products of photocatalytic CO_2 reduction on perovskite QDs are CO and CH_4. Besides, some similar thermodynamic potentials of products induce several side reactions and low selectivity, such as CO_2 reduction to CH_3OH and CO, or direct reduction of $2H^+$ to H_2.[4]

2.3 Obstacles for photocatalytic CO_2 reduction

Although halide perovskite QDs have unique physical and chemical properties, the intrinsic structural instability and high carrier recombination rate limit their practical application in photocatalytic CO_2 reduction.

2.3.1 Structural instability. Structural instability is a big obstacle for widespread application of perovskite QDs. The intrinsic ionic properties allow perovskite QD synthesis under very moderate conditions. The typical hot-injection method to
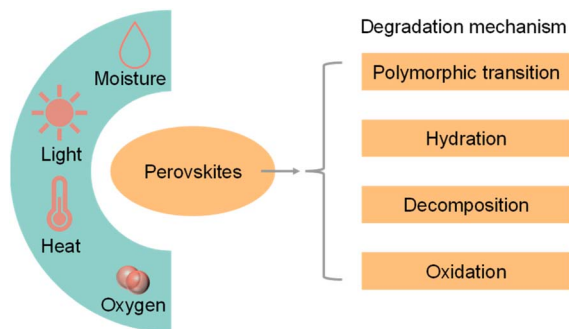
synthesize perovskite QDs occurs below 200 °C. Another method to prepare perovskite QDs is the ligand-assisted re-precipitation method, where the solution of the corresponding ions in a polar solvent is quickly added into a non-polar solvent, resulting in rapid nucleation and growth.[35] However, despite easy synthesis of perovskite QDs, the intrinsic instability brings a big challenge for their practical applications. First, perovskite QDs are terminated by long-chain organic ligands (oleylammonium bromide and oleylammonium carboxylate). However, these anchoring ammonium and carboxylate groups are prone to desorption from the surface, which easily forms defects and accelerates halide migration.[44] Even the isolation and purification processes would induce the desorption of ligands and structural instability. Secondly, the intrinsic ionic features and surficial lability make perovskites quickly soluble in a polar solvent and lose the perovskite lattice structure.[45] Thus, the instability of halide perovskite QDs has inspired many efforts and developments to boost long-term stability for photocatalysis.[46,47] A straightforward method is to exploit the chemical equilibrium to stabilize perovskite via saturated halide acid solution with the corresponding halide perovskite. In 2016, Nam and co-workers utilized $MAPbI_3$ to realize stable photocatalytic H_2 production in saturated hydrogen iodide acid solution for the first time.[48] It was found that the concentrations of I^- and H^+ were the critical parameters to stabilize the tetragonal $MAPbI_3$ phase and achieve long durability for solar-driven hydrogen production. In 2017, Su et al. found that $CsPbBr_3$ could remain stable in ethyl acetate and perform photocatalytic CO_2 reduction.[18] In low-polarity solvents (e.g., ethyl acetate, acetonitrile, and toluene), perovskite materials would not dissociate because of the relatively weak dipole moment of the solvent. After illumination for 12 h, pristine $CsPbBr_3$ QDs could generate 49.5 $\mu mol\ g^{-1}$ CO and 22.9 $\mu mol\ g^{-1}$ CH_4, respectively, while the $CsPbBr_3$/graphene oxide (GO) composite produced 58.7 $\mu mol\ g^{-1}$ CO and 29.6 $\mu mol\ g^{-1}$ CH_4, respectively. Inspired by this strategy, research on photocatalytic CO_2 reduction of halide perovskite QDs boomed rapidly.[24,49]

Apart from instability in a polar solvent, perovskite materials would also decompose rapidly when exposed to moisture, heat, light, and oxygen.[50] Fig. 5 shows the environmental factors and possible degradation mechanisms of perovskite materials.[51] The common degradation mechanisms of perovskite materials include polymorphic transformation, hydration,

Fig. 4 Band edge positions of traditional photocatalysts and different halide perovskites relative to the reversible hydrogen electrode (RHE). Reproduced from ref. 25 and ref. 26 with permission from American Chemical Society, copyright 2022.

12486 | J. Mater. Chem. A, 2023, **11**, 12482–12498

This journal is © The Royal Society of Chemistry 2023

Fig. 5 Scheme of the environmental factors (moisture, light, heat, and oxygen) and possible degradation mechanisms of perovskite materials. Reproduced from ref. 51 with permission from Elsevier, copyright 2018.

decomposition, and oxidation. Unlike organic–inorganic hybrid perovskite QDs, all-inorganic perovskite QDs do not have hygroscopic organic cations. Hence, all-inorganic perovskite QDs would not be degraded by hydration.[52] Long-term light irradiation would cause the desorption of surficial ligands, transportation of halide ions and accumulation of NCs.[53] These processes originated from the rapid formation of halide vacancies after light illumination, providing a path for oxygen or water molecules into the perovskite lattice.[54] It is also a great challenge for halide perovskite materials to operate at a high temperature. Hybrid organic–inorganic perovskite QDs decompose before melting (melting point: $MAPbI_3$: 150–200 °C; $FAPbI_3$: 290–300 °C), while the melting point of the all-inorganic QDs are higher ($CsPbBr_3$ and $CsPbI_3$: 450–500 °C).[35] In addition, perovskite QDs would be stable only for an extremely low oxygen concentration, because high oxygen partial pressures could generate reactive intermediates such as superoxide species under light illumination.[55,56]

Another unignorable factor for perovskite instability is the phase transition at room temperature, especially for $CsPbI_3$. The photoactive cubic phase of perovskite (α-$CsPbI_3$) would spontaneously undergo phase transition to the non-perovskite phase (δ-$CsPbI_3$) owing to the lower formation energy of δ-$CsPbI_3$. Only the photoactive perovskite phase can absorb visible light and show good photocatalytic activity for CO_2 reduction. Some studies would incorporate the ions with a larger radius into the A-site (such as, FA and MA) or replace I^- with Br^- to stabilize α-$CsPbI_3$ QDs.[44,57]

2.3.2 Carrier recombination. The fast carrier recombination of perovskite QDs is another fatal flaw for photocatalytic CO_2 reduction. A good photocatalyst ought to have a large light absorption coefficient, effective charge separation and transfer, a low carrier recombination rate, and a long carrier diffusion distance. Among these steps, charge separation and transfer predominate the whole photocatalytic reaction. Charge separation and recombination are comparative processes, and the time scales of the recombination lifetime and charge transfer are within nanoseconds. Thus, how to achieve fast charge transfer is very essential for photocatalysis. Nonetheless, the high quantum efficiency of perovskite QDs implies that the

photogenerated electron–hole pairs would recombine rapidly, which is unfavourable for photocatalytic CO_2 reduction. Some measures have been taken to boost charge transfer and separation. For example, *via* constructing a heterojunction, photogenerated electrons and holes could migrate to different materials, leading to spatial separation of photogenerated carriers.[28]

3. Current strategies for perovskite photocatalytic CO_2 reduction

Even though halide perovskite QDs have been widely utilized for solar cells,[58] research on perovskite QDs for photocatalysis is still in the initial stage. In the former parts, we understood the mechanism and obstacles of perovskite QDs for photocatalytic CO_2 reduction from the fundamental and basic properties. Herein, recent progress and successful strategies to improve photocatalytic performance and stability are given in the following sections, including composition optimization (doping, bandgap adjustment, and morphology regulation), surface modification (ligand modification, oxide encapsulation, and MOF encapsulation) and heterostructure construction (Schottky heterojunction, type II heterojunction, and *Z*-scheme heterojunction).

3.1 Composition optimization

The intrinsic physical and chemical properties of a photocatalyst influence its photocatalytic performance. For a photocatalyst, its intrinsic composition involves the band structure, bandgap, charge transfer, crystal face, active site, and so on. Doping, bandgap adjustment, and morphology regulation are general measures to optimize the intrinsic composition and improve the photocatalytic activity for CO_2 reduction.[59,60]

3.1.1 Doping. It is well-known that doping is an effective and simple method to regulate photocatalyst properties.[61] A doping atom can occupy and substitute a lattice atom or become an interstitial atom.[62] Fig. 6a shows the conventional doping elements of A-site and B-site cations in perovskite materials. Chen *et al.* doped Mn^{2+} into $CsPbBr_3$ to enhance photocatalytic CO_2 reduction efficiency of perovskite QDs (Fig. 6b).[59] The Mn-doped $CsPbBr_3$ nanoplates showed remarkable product yields of CO (45.4 μmol g^{-1}) and CH_4 (3.5 μmol g^{-1}) compared to pristine $CsPbBr_3$ owing to spin-polarized electrons from Mn doping. By applying a 300 mT magnetic field, Mn-doped $CsPbBr_3$ could display a 5.7-fold improvement in photocatalytic CO_2 reduction from the increased spin-polarized photoexcited carriers by synergistic doping of the magnetic elements on applying a magnetic field. In addition, other metal atoms (Cd^{2+},[63] Cu^{2+},[64] Zn^{2+},[65] and so on) have also been successfully doped into halide perovskite QDs. Li and co-workers used the surface segregation effect to synthesize stable Bi-doped $CsPbCl_3$ NCs with a core–shell structure, and the segregation effect formed a low Bi-doping region and high Bi-doping region.[66] Density functional calculations (DFT) were performed to study the electronic structure of Bi-doped $CsPbCl_3$. Theoretical calculations revealed that Bi dopants
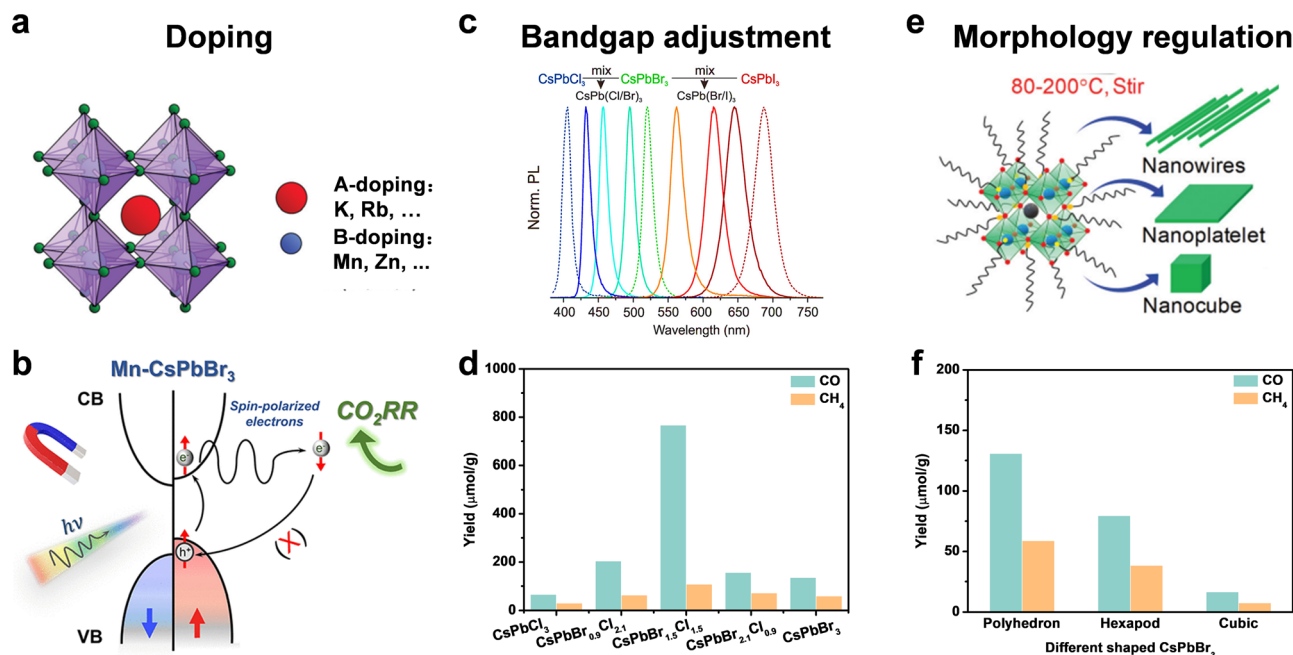
This journal is © The Royal Society of Chemistry 2023

J. Mater. Chem. A, 2023, **11**, 12482–12498 | **12487**

Fig. 6 (a) Doping: A–site doping and B–doping; reproduced from ref. 62 with permission from Royal Society of Chemistry, copyright 2020. (b) Suppressed electron spin polarization of Mn doped $CsPbBr_3$; reproduced from ref. 59 with permission from American Chemical Society, copyright 2022. (c) Bandgap adjustment: halide ratio; reproduced from ref. 12 with permission from American Chemical Society, copyright 2015. (d) Yields of CO_2 reduction under 9 h Xe lamp irradiation with AM 1.5; reproduced from ref. 74 with permission from Elsevier, copyright 2015. (e) Morphology regulation: nanowires, nanoplatelets, and nanocubes; reproduced from ref. 75 with permission from Royal Society of Chemistry, copyright 2020. (f) Yields of CO and CH_4 from CO_2 reduction after 4 h using different shaped $CsPbBr_3$ nanostructures; reproduced from ref. 77 with permission from American Chemical Society, copyright 2020.

narrowed the bandgap of $CsPbCl_3$ NCs. Meanwhile, the result of ultrafast transient absorption spectroscopy indicated that the surficial gradient distribution of Bi atoms led to a fast tunnel and promoted photogenerated carrier transfer from the core to the shell region. This special core–shell structured Bi-doped $CsPbCl_3$ exhibited a stable crystal structure and morphology, enabling long-term stability for photocatalytic CO_2 reduction. After cycling tests under light irradiation and high humidity, the Bi-doped $CsPbCl_3$ NCs could maintain 97% of its original photocatalytic activity, while the photocatalytic activity of pristine $CsPbCl_3$ NCs was reduced by about 92%. This strategy paved a new way to construct a highly efficient and stable perovskite photocatalyst.

Although an A-site cation was thought to hardly influence optoelectronic properties of perovskite materials, some recent studies have confirmed that A-site doping (such as K^+,[67] Rb^+,[68,69] and so on) could improve stability and facilitate carrier transport. Because X-site anions directly affect the bandgap, we will discuss the X-site dopants in bandgap adjustment.

3.1.2 Bandgap adjustment. For photocatalysis, the semiconductor bandgap and band structure determine the light absorption range and redox potential, which has a decisive effect on photocatalytic performance. Because Pb-based perovskite materials have high toxicity for the environment and surroundings, Bi-based, Sn-based, and double perovskite materials gradually emerged.[70,71] Taking double perovskite Cs_2AgBiX_6 as an example, M. A. Amin *et al.* used DFT to

calculate the band structure of Cs_2AgBiX_6.[72] The result showed that the d states of Ag and p states of the X atom with minor s states of Bi contributed to the VB, and the CB came from the p states of Bi with small addition of s, p, and d states of Ag. The bandgaps were 2.76 eV and 1.90 eV for $Cs_2AgBiCl_6$ and $Cs_2AgBiBr_6$, and 2.9 eV and 2.4 eV for $CsPbCl_3$ and $CsPbBr_3$, respectively. Compared to $CsPbX_3$, the narrower bandgaps and greener composition of Cs_2AgBiX_6 held great advantages for highly efficient photocatalytic CO_2 reduction. Chen's group prepared high-quality two-dimensional Cs_2AgBiX_6 nanoplates with a room temperature precursor injection followed by a solution heating up process.[73] During 6 hours of visible-light illumination, the $Cs_2AgBiBr_6$ nanoplates displayed 255.4 μmol g^{-1} electron consumption for photocatalytic CO_2 reduction to CO and CH_4, demonstrating high reaction activity of 2D lead-free perovskite materials for photocatalytic CO_2 reduction.

Another strategy to optimize the bandgap is to change the halide ratio. As shown in Fig. 6c, through different halide compositions, the emission spectra can be easily changed over the full-visible wavelength of 410–700 nm.[12] Su *et al.* synthesized $CsPbCl_xBr_{3-x}$ NCs with different ratios of Br and Cl by the hot-injection method.[74] The yield of photocatalytic CO_2 reduction to CO and CH_4 varied with the ratio of Br and Cl. $CsPbBr_{1.5}Cl_{1.5}$ exhibited the highest yield of CO (767 μmol g^{-1}) and CH_4 (108 μmol g^{-1}), a nearly 4.5- and 9.1-fold enhancement compared to that of pristine $CsPbBr_3$ and $CsPbCl_3$ under the same conditions for 9 h irradiation (Fig. 6d), attributed to the efficient

12488 | *J. Mater. Chem. A*, 2023, **11**, 12482–12498

This journal is © The Royal Society of Chemistry 2023

photogenerated carrier migration and separation of $CsPbBr_{1.5}Cl_{1.5}$ NCs.

3.1.3 Morphology regulation. As different morphological structures and crystal faces of halide perovskite QDs can affect the surficial active sites, CO_2 adsorption and electron migration ability, it is of great interest to develop morphological dimensionality-controlled perovskite materials to explore shape- and facet-dependent photocatalytic properties (Fig. 6e).[75] Perovskite QDs have an obvious quantum confinement effect because the particle size is smaller than the Bohr radius.[35] When the hot-injection method was used to synthesize perovskite QDs, the particle size was increased with increasing temperature. Due to the quantum confinement effect, different particle sizes would have different bandgaps and thus varied photocatalytic performances. Sun et al. found that perovskite QDs had size-dependent activity for CO_2 reduction.[76] They utilized different sizes (3.8, 6.1, 8.5, and 11.6 nm) of $CsPbBr_3$ QDs for photocatalytic CO_2 reduction under the same experiment conditions and found that the 8.5 nm QDs showed the highest yields for CO (34.1 μmol g^{-1}) and CH_4 (12.2 μmol g^{-1}) production after 8 h illumination.

Different facets and crystal orientations have different active sites and surface energy. A good crystal face should enable the efficient adsorption of reactants and the desorption of products. Besides, the photogenerated electrons and holes tend to accumulate on different facets, leading to facet-dependent photocatalytic properties. Pradhan and cooperators explored the polyhedron-shaped nanocubes, hexapods, and cube-shaped $CsPbBr_3$ nanostructure for CO_2 photoreduction.[77] As shown in Fig. 6f, the polyhedron-shaped nanocubes exhibited the best photocatalytic activity (130.7 μmol g^{-1} for CO and 58.7 μmol g^{-1} for CH_4 for 4 h) due to the fastest charge transfer for photocatalysis. TEM images showed polyhedron shapes had eight {112}, eight {012}, and four {100} prominent facets, while cube shapes were composed of four {110} and two {002} facets. DFT calculations showed that {112} and {102} facets were more superior for surface adsorption of CO_2 and desorption of reduction products compared to the dominant {110} and {002} facets of orthorhombic cube shaped $CsPbBr_3$. As facets affect photocatalytic performance, different facets of perovskite QDs should be further studied for efficient catalytic reaction.

It is noteworthy that the formation process of perovskite QDs is within sub-seconds through hard-to-control ionic metathesis nucleation and the growth process. Kovalenko's group reported a room-temperature method to fabricate monodisperse and isolable perovskite QDs with sizes from 3 to 13 nm.[78] The processes of nucleation and growth were slowed down to 30 min by using trioctylphosphine oxide (TOPO) complexing with $PbBr_2$ as the monomer of the $Cs[PbBr_3]$ solute and adding a long-chain zwitterion-lecithin at the end of formation. The slower nucleation and growth processes could be observed by in situ optical absorption and emission spectroscopy. The controllable synthesis of perovskite QDs will encourage researchers to obtain desirable facets for photocatalysis, which further helps understand the relationships between different facets of perovskite QDs and catalytic performance.

3.2 Surface modification

The surface states of semiconductors represent termination of the periodic arrangement of crystals. This would generate dangling bonds on the surface and alter the surficial band structure. Hence, the crystal surface state can affect surface energy, coordination number, molecular adsorption, interface carrier transfer, and so on. In this section, we focus on ligand modification and encapsulation to improve the stability and photocatalytic performance of halide perovskite QDs.

3.2.1 Ligand modification. Surface ligands play a crucial role in the formation of perovskite QDs, which not only influence the nucleation and growth processes, but are also extremely essential for charge migration and structural stability.[79] Generally, long-chain oleic acid (OA) and oleylamine (OAm) are added as surface ligands to synthesize perovskite QDs. The OA/OAm ligands would easily desorb from the surface and generate many defects, which further induce halide migration and segregation. Such OA/OAm-capped perovskite QDs are unstable, and gradually undergo structural decomposition.[80] In addition, the long-chain and insulative OA/OAm ligands are not beneficial for photogenerated carrier transfer. Both instability and low conductivity prevent the practical photocatalysis of perovskite QDs. Thus, how to design suitable ligands to replace the typical long-chain OA and OAm is a challenge.

Although many studies have utilized organic molecules as ligands to improve the stability of perovskite QDs and passivate the surface defects, it seemed that most studies also enhanced radiative recombination and fluorescence intensity.[81] As depicted in Fig. 7a, common passivated organic molecules include alkylammonium salts, alkylcarboxylic/alkylphosphonic/alkylsulfonic acids, thiol/thiolate, zwitterionic molecules, and so on.[82,83] However, to realize the application in photocatalysis, the specific modified ligands should boost the stability and facilitate carrier transfer simultaneously.[84] Li et al. used thionyl bromide ($SOBr_2$) to promote the stripping of original ligands (OA/OAm) and compensate Br vacancies on $CsPbBr_3$ NCs to improve the stability, which could also facilitate the charge transfer and separation from $CsPbBr_3$ to g-C_3N_4 (Fig. 7b).[27] $CsPbBr_3$–$SOBr_2$ showed an enhanced CO_2 reduction activity (total electron consumption: 69 μmol g^{-1} h^{-1}), which was about 6-fold higher than that of pristine $CsPbBr_3$. After further combination with g-C_3N_4, the photocatalytic CO_2 yield reached 190 μmol g^{-1} h^{-1}. Li et al. selected tetrafluoroborate salts (BF_4^-) as a defect treatment agent and then loaded Co^{2+} as a cocatalyst.[85] The result showed that $CsPbBr_3$–BF_4 had a photocatalytic CO_2 performance of 83.8 μmol g^{-1} h^{-1} electron consumption, demonstrating that such surface molecules could reduce carrier recombination and facilitate charge separation.

3.2.2 Encapsulation. Due to the vulnerability of perovskite QDs to moisture, oxygen, and heat, encapsulating them with a more stable substance is a straightforward strategy to improve their stability. So far, many studies have used SiO_2 to encapsulate perovskite QDs to promote the structural stability of perovskite QDs.[86] However, this also prevented effective electron migration and could not be applied for photocatalysis. To
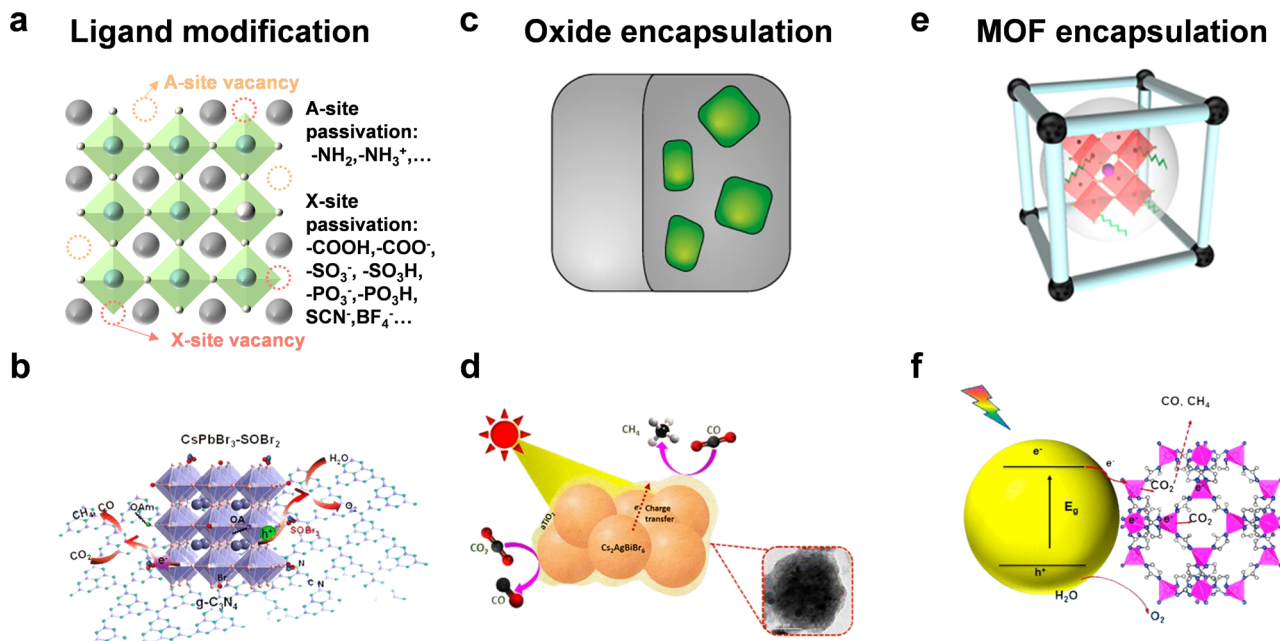
This journal is © The Royal Society of Chemistry 2023

J. Mater. Chem. A, 2023, **11**, 12482–12498 | **12489**

Fig. 7 (a) Ligand modification; reproduced from ref. 83 with permission from Springer Nature, copyright 2020. (b) $CsPbBr_3$ with $SOBr_2$ modification for photocatalytic CO_2 reduction; reproduced from ref. 27 with permission from American Chemical Society, copyright 2022. (c) Oxide encapsulation; reproduced from ref. 35 with permission from Springer Nature, copyright 2018. (d) Photocatalytic CO_2 reduction of TiO_2-encapsulated $Cs_2AgBiBr_6$ NCs; reproduced from ref. 87 with permission from American Chemical Society, copyright 2022. (e) MOF encapsulation; reproduced from ref. 91 with permission from Wiley-VCH, copyright 2022. (f) $CsPbBr_3$@zeolitic nanocomposite for photocatalytic CO_2 reduction. Reproduced from ref. 92 with permission from American Chemical Society, copyright 2018.

broaden the application for photocatalysis, it is necessary to select conductive materials for encapsulation.

A protective layer of metal oxide can isolate perovskite QDs from the external environment and benefit charge transfer (Fig. 7c). As shown in Fig. 7d, Satapathi *et al.* fabricated amorphous TiO_2-coated $Cs_2AgBiBr_6$ NCs *via* the anti-solvent recrystallization method.[87] In contrast with pristine $Cs_2AgBiBr_6$, the $Cs_2AgBiBr_6$-amorphous TiO_2 nanocomposite showed an 11-fold enhancement of CO (22.87 μmol g^{-1}) and CH_4 (33.86 μmol g^{-1}) production for 2 h reaction because of more efficient charge separation and transfer. Some other oxide semiconductors, such as SnO_2,[88] and ZnO,[89] also allow great potential for photocatalytic CO_2 reduction.

Metal organic frameworks (MOFs) are good candidates for photocatalytic CO_2 reduction because of the controllable porous structure, high surface area, superior conductivity, and adsorption ability.[90] The integration of MOFs and perovskite QDs offers more possibilities for CO_2 transformation into valuable products (Fig. 7e).[91] Su's group designed cobalt-based zeolitic imidazolate frameworks (ZIFs) to coat on the surface of $CsPbBr_3$ QDs (Fig. 7f).[92] The coated ZIFs could promote CO_2 activation and improve CO_2 photoconversion as a co-catalyst for photocatalysis. After optimization, $CsPbBr_3$@ZIF-8 and $CsPbBr_3$@ZIF-67 displayed total electron consumption rates of 15.498 and 29.630 μmol g^{-1} h^{-1}, respectively, which were 1.39- and 2.66-fold higher than that of $CsPbBr_3$ QDs.

Besides, some conductive materials have also been used to coat perovskite QDs for photocatalytic CO_2 reduction. For example, MXenes, a member of 2D conductive materials, was

utilized to encapsulate $Cs_2AgBiBr_6$ NCs to facilitate efficient charge separation and transport.[93] To conclude, surface modification is an effective measure to maintain structural stability of perovskite QDs. If these nanocomposites are applied for photocatalysis, it is necessary that these ligands or coating materials can facilitate charge migration and separation.

3.3 Heterojunction construction

To promote photogenerated carrier transfer and separation, many scientists have constructed a series of interfacial heterojunctions. Because of the carrier confinement effect of a type-I heterojunction and without synergistic effects of a type-III heterojunction, they are not preferable for photocatalysis and will not be discussed in this section. Here, we mainly focus on these heterojunctions: a Schottky heterojunction, type-II heterojunction, direct *Z*-scheme heterojunction, and all-solid *Z*-scheme heterojunction, as shown in Fig. 8. Recently, many reports have fabricated different types of perovskite-based heterostructures for photocatalytic CO_2 reduction,[94,95] which are further summarized and discussed below.

3.3.1 Schottky heterojunction. Schottky heterojunctions are formed by the interface region between metallic materials and semiconductors. The formation mechanism of a Schottky heterojunction is attributed to the fact that the Fermi level of semiconductors is higher than that of metallic materials. After illumination, the photogenerated electrons would be transferred from semiconductors to metallic materials for a reduction reaction, and the photogenerated holes would stay in the
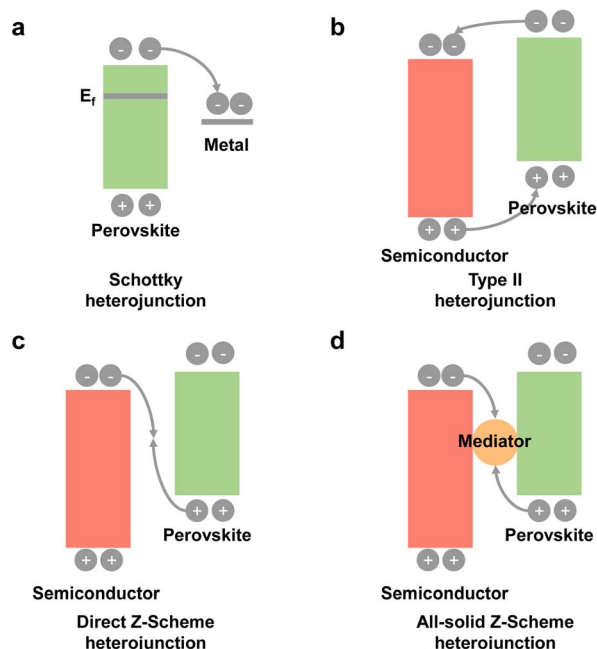
12490 | *J. Mater. Chem. A*, 2023, 11, 12482–12498

This journal is © The Royal Society of Chemistry 2023

Fig. 8 Schematic illustration of heterojunctions under irradiation: a (a) Schottky heterojunction; (b) type II heterojunction; (c) direct Z-scheme heterojunction; (d) all-solid Z-scheme heterojunction. E_f: work function.

Fig. 9 (a) CsPbBr$_3$/Pd nanosheet Schottky junction for CO$_2$ reduction; reproduced from ref. 98 with permission from American Chemical Society, copyright 2018. (b) Photocatalytic CO$_2$ reduction performances after 3 h of constant illumination; 100, 300, 600, and 900 mean the volume (μL) of added Pd nanosheets; CsPbBr$_3$: abbreviated as CPB; reproduced from ref. 98 with permission from American Chemical Society, copyright 2018. (c) Cs$_2$SnI$_6$/SnS$_2$ nanosheet type-II heterojunction for CO$_2$ reduction; reproduced from ref. 106 with permission from American Chemical Society, copyright 2010. (d) Photocatalytic CO$_2$ reduction to CH$_4$ of SnS$_2$, Cs$_2$SnI$_6$(0.5)/SnS$_2$, Cs$_2$SnI$_6$(1.0)/SnS$_2$, and Cs$_2$SnI$_6$(2.0)/SnS$_2$ nanocomposites; 0.5, 1.0, and 2.0 correspond to the concentration (1.0 mM, 2.0 mM, and 4.0 mM) of CsI; reproduced from ref. 106 with permission from American Chemical Society, copyright 2019.

semiconductors for an oxidation reaction, which leads to effective charge separation and reduces undesirable radiative recombination.[96] Su's group constructed a CsPbBr$_3$/Au Schottky heterojunction and then used Al-based mesoporous MOF particles to encapsulate CsPbBr$_3$/Au NCs for synergetic photocatalytic CO$_2$ reduction.[97] Optical and photoelectrical characterization studies confirmed that the photogenerated electrons could migrate from CsPbBr$_3$ to Au and strongly inhibit charge recombination. The electron consumption of CsPbBr$_3$/Au/PCN-333(Al) nanoparticles showed a nearly 11.5-fold enhancement than that of pristine CsPbBr$_3$ NCs. Similarly, as shown in Fig. 9a, Kuang *et al.* also reported a CsPbBr$_3$/Pd Schottky heterostructure for photocatalytic CO$_2$ reduction.[98] After optimization, the highest electron consumption rate reached 33.80 μmol g^{-1} h^{-1} with 600 μL of Pd nanosheets, which was a 2.43-fold enhancement compared to that of pristine CsPbBr$_3$ (Fig. 9b).

Some reports found that the surface plasmon resonance (SPR) effect caused by the interaction between the incident photons and the conduction electrons of metal nanoparticles also contributed to photocatalysis.[99,100] Kuang and cooperators synthesized Au decorated CsPbBr$_3$ nanoparticles.[101] Under light illumination ($\lambda > 420$ nm), photogenerated electrons could be transferred from CsPbBr$_3$ to Au, but when irradiated with longer wavelength light ($\lambda > 580$ nm), the induced hot electrons of Au from the SPR effect could be transferred to CsPbBr$_3$ and further facilitate photocatalytic CO$_2$ reduction. Besides, prolonged stability of the Schottky heterostructure is also a big issue.[102] After long-term irradiation, the precious metal nanoparticles would accumulate and induce a drop in photocatalytic activity.
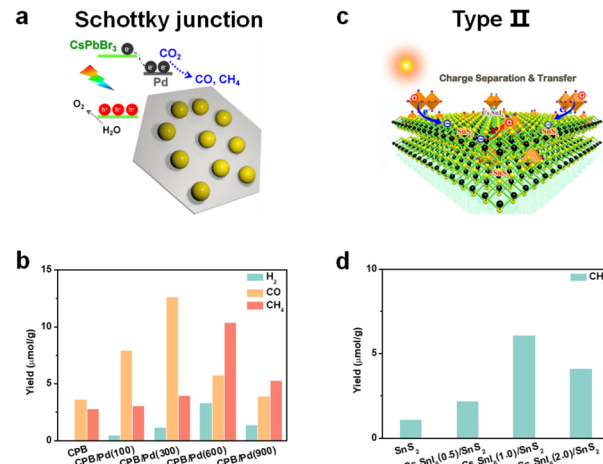
Thus, the use of precious metals to construct Schottky heterojunctions deserves more attention.

3.3.2 Type-II heterojunction. As shown in Fig. 8b, a type-II heterojunction is constructed by two semiconductors with a staggered band alignment. Under light irradiation, the photogenerated electrons would be transferred from the material with a higher CB to the material with a lower CB for reduction, and the photogenerated holes would be transferred from the material with a lower VB to the material with a higher VB for oxidation. The photogenerated electrons and holes accumulate in different semiconductors, which leads to effective spatial separation of carriers.[103] So far, many perovskite-based type-II heterojunctions have been reported for photocatalysis, such as CsPbBr$_3$/TiO$_2$,[104] CsPbBr$_3$/ZnSe,[53] and CsPbBr$_3$/g-C$_3$N$_4$.[20]

Gong's group synthesized a 0D/0D type-II CsPbBr$_3$/CdSe heterojunction by an *in situ* growth method.[105] DFT calculations showed that there was a strong electronic coupling of Pb–Se and Br–Cd bonds, which facilitated fast electron transfer and separation. *In situ* diffuse reflectance infrared Fourier transform spectroscopy (DRIFTS) found that the intermediate Cd–C$_2$O$_4^-$ adduct could enable efficient CO$_2$ activation and accelerate CO production. With the help of water to provide electrons and protons, the yield of CO reached 115.26 μmol g^{-1} under visible light illumination for 3 h, which was about 4.6-fold higher than that of CsPbBr$_3$ QDs. Kuang *et al.* constructed hybrid Cs$_2$SnI$_6$/SnS$_2$ nanosheets *via in situ* synthesis for the first time (Fig. 9c).[106] Ultraviolet photoelectron spectroscopy (UPS)

This journal is © The Royal Society of Chemistry 2023

J. Mater. Chem. A, 2023, **11**, 12482–12498 | **12491**

analysis and theoretical calculations showed that the co-sharing of a Sn atom makes Cs_2SnI_6/SnS_2 come into intimate contact with a type-II heterojunction. Under visible-light illumination, the CH_4 yield of Cs_2SnI_6/SnS_2 was 6.09 μmol g^{-1}, nearly 5.4 times higher than that of SnS_2 (Fig. 9d), which originated from the improved light absorption and charge separation after incorporation of Cs_2SnI_6.
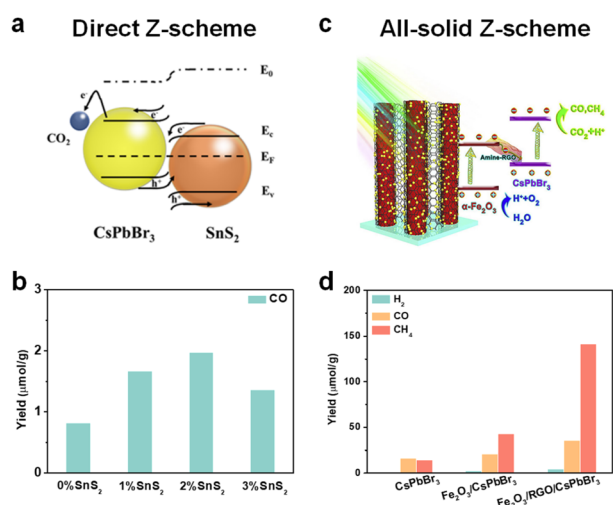
3.3.3 Z-scheme heterojunction. A Z-scheme heterojunction also consists of two semiconductors with a staggered band alignment. Nonetheless, the photogenerated electrons from the semiconductor with a lower CB would recombine with the photogenerated holes from the semiconductor with a higher VB. Hence, higher redox potentials would be preserved for photocatalysis.[107] According to the presence or absence of mediators, the Z-scheme can be divided into direct Z-scheme and all-solid Z-scheme.

Even though it is not easy to construct a Z-scheme heterojunction, some reports have successfully fabricated a Z-scheme heterojunction. Xie *et al.* synthesized a series of $SnS_2/CsPbBr_3$ heterostructures for photocatalytic CO_2 reduction (Fig. 10a).[107] Interface and surface carrier dynamic investigations confirmed that the $SnS_2/CsPbBr_3$ heterojunctions satisfied direct Z-scheme transfer dynamics and could effectively improve carrier separation efficiency. As shown in Fig. 10b, $SnS_2/CsPbBr_3$ showed much higher CO production than pristine $CsPbBr_3$ (marked as 0% SnS_2 in Fig. 10b). Li's group used $Cs_2AgBiBr_6$ and Sr_2FeNbO_6 to construct a Z-scheme heterostructure.[108] *In situ* light-irradiation X-ray photoelectron spectroscopy (XPS) spectra and

theoretical calculations confirmed that the $Cs_2AgBiBr_6/Sr_2FeNbO_6$ composites belonged to a direct Z-scheme heterojunction. With the irradiation of visible light ($\lambda \geq 420$ nm), the photocatalytic CO and CH_4 yields reached 50.00 and 8.12 μmol g^{-1} h^{-1}, respectively. Li's group also fabricated a 0D/2D $Cs_2AgBiBr_6/Bi_2WO_6$ heterojunction, and the photocatalytic results showed that the $Cs_2AgBiBr_6/Bi_2WO_6$ heterojunction achieved 7-fold higher activity than pristine $Cs_2AgBiBr_6$ under simulated solar light (AM 1.5G).[109] Besides, the $CsPbBr_3/Bi_2WO_6$ Z-scheme heterojunctions have also been reported.[19,110]

In addition, a perovskite-based all-solid Z-scheme heterojunction has also been reported. As shown in Fig. 10c, Kuang *et al.* constructed a $CsPbBr_3$/reduced graphene oxide (RGO)/Fe_2O_3 Z-scheme heterojunction for photocatalytic CO_2 reduction.[110] The effective Z-scheme electron transfer path from the CB of Fe_2O_3 to the VB of $CsPbBr_3$ was confirmed by electron spin resonance (ESR) analysis. Under irradiation, photogenerated electrons and holes could be effectively separated for CO_2 reduction at $CsPbBr_3$ and H_2O oxidation at Fe_2O_3, respectively. In contrast with $CsPbBr_3$ and $Fe_2O_3/CsPbBr_3$, this effective photogenerated carrier separation and transfer of the Z-scheme Fe_2O_3/Amine-RGO/$CsPbBr_3$ heterojunction enabled highly efficient CO_2 photoreduction. As depicted in Fig. 10d, after 15 h irradiation, the Fe_2O_3/Amine-RGO/$CsPbBr_3$ heterojunction had the highest yield of CO (35.47 μmol g^{-1}) and CH_4 (141.81 μmol g^{-1}).

In short, the Z-scheme heterojunction shows tremendous advantages for photocatalysis owing to high redox potential, high-efficiency charge separation, and wide light-harvesting. However, the construction of a Z-scheme heterojunction is very complicated on account of interfacial interaction, the internal electric field, and band energy requirement.

4. Challenges and opportunities

Due to remarkable photophysical and photochemical properties, halide perovskite QDs display great potentials for photocatalytic CO_2 reduction, as summarized in Table 1. However, severe instability and charge recombination inhibit the photocatalytic CO_2 reduction of perovskite QDs. Although some useful strategies have been carried out and some progress has been made for photocatalytic CO_2 reduction, many challenges should also be highlighted and addressed before practical application, such as, long-term stability, Pb-free perovskite, Z-scheme formation scheme, and theoretical calculations (Fig. 11).

4.1 Long-term stability

The intrinsic ionic properties of halide perovskite materials lead to high instability in a polar solvent.[111–113] The labile ligands are easily desorbed from the surface of perovskite QDs. All these problems would affect the long-term stability of a perovskite photocatalyst. To promote structural stability of perovskite QDs, exploiting suitable ligands to substitute OA/OAm is a feasible strategy. However, many reported studies focus on passivating surface defects, reducing non-radiative

Fig. 10 (a) Direct Z-scheme $SnS_2/CsPbBr_3$ heterojunction for CO_2 reduction; reproduced from ref. 107 with permission from Wiley-VCH, copyright 2022. (b) Photocatalytic CO_2 reduction performance of $SnS_2/CsPbBr_3$ heterojunctions under illumination; the percentage represents the added SnS_2; reproduced from ref. 107 with permission from Wiley-VCH, copyright 2022. (c) All-solid-state Z-scheme α-Fe_2O_3/Amine-RGO/$CsPbBr_3$ heterojunctions for photocatalytic CO_2 reduction; reproduced from ref. 110 with permission from Elsevier, copyright 2020. (d) Photocatalytic CO_2 reduction performances of $CsPbBr_3$, α-$Fe_2O_3/CsPbBr_3$, and α-Fe_2O_3/Amine-RGO (RGO)/$CsPbBr_3$ after 15 h irradiation; reproduced from ref. 110 with permission from Elsevier, copyright 2020.

12492 | *J. Mater. Chem. A*, 2023, **11**, 12482–12498

This journal is © The Royal Society of Chemistry 2023

Table 1 Summary of the photocatalytic CO_2 reduction performance of perovskite QDs under various light sources

Photocatalyst	Light source	Solution	Product ($\mu mol\ g^{-1}\ h^{-1}$)	Measured stability	Ref.
$CsPbBr_3$	100 W Xe lamp, AM 1.5G	Ethyl acetate	CO, 4.3 CH_4, 1.5 H_2, 0.1	8 h	76
$CsPbBr_3$/GO	100 W Xe lamp AM 1.5G, 150 mW cm^{-2}	Ethyl acetate	CO, 4.9 CH_4, 2.5 H_2, 0.13	12 h	18
$Cs_2AgBiBr_6$/MXene	300 W Xe lamp, 420 nm filter	Water vapor	CO, 11.1 CH_4, 1.3 H_2, 8.9	5 h	93
$CsPbBr_3$@ZIF-67	100 W Xe lamp, AM 1.5G, 150 mW cm^{-2}	Water vapor	CO, 0.77 CH_4, 3.51	18 h	92
Cs_2SnI_6/SnS_2	150 mW cm^{-2} visible light, 400 nm filter	Water/methanol vapor	CH_4, 6.09	9 h	106
Cd : $CsPbBr_3$	450 W Xe lamp, AM 1.5G, 150 mW cm^{-2}	Ethyl acetate/water	CO, 12.6 CH_4, 26.5	8 h	130
$CsPbBr_{3-x}Cl_x$	300 W Xe lamp, AM 1.5G, 200 mW cm^{-2}	Ethyl acetate	CO, 85, CH_4, 12	8 h	74
$Cs_3Bi_2Br_9$/TiO_2	300 W Xe lamp, AM 1.5G, 70 mW cm^{-2}	Isopropanol	CO, 4.2 CH_4, 32.9	7 h	23
$CsPbBr_3$/CdSe	300 W Xe lamp, AM 1.5G, 420 nm filter, 150 mW cm^{-2}	Ethyl acetate/H_2O	CO, 38.4 CH_4, 8.5	9 h	105
α-Fe_2O_3/Amine-RGO/$CsPbBr_3$	150 W Xe lamp, AM 1.5G, 420 nm filter, 150 mW cm^{-2}	Water vapor	CO, 2.4 CH_4, 9.5 H_2, 0.3	40 h	110

recombination, and improving stability, which have been applied for LEDs and solar cells. Thus, it is necessary to design a suitable conductive ligand to improve long-term stability and facilitate charge transfer simultaneously.[114] For instance, poly [(thiophene)-alt-(6,7-difluoro-2-(2-hexyldecyloxy)-quinoxaline)], a stable and conjugated molecule, has been used to improve the stability and efficiency of perovskite solar cells.[115]

In fact, one of the most effective strategies is to construct a core–shell structure, which can preserve perovskite QDs from outer adverse environments. Unfortunately, recent studies just utilized perovskite-based core–shell nanoparticles to improve water-resistivity. Because of insulation or band misalignment, it seems that these shells cannot realize charge transfer and separation. Furthermore, the synthesis of perovskite-based core–shell nanoscale heterostructures has not been realized. A stable conductive shell can maintain the structural stability of core perovskite QDs and facilitate electron transfer for photocatalytic CO_2 reduction. Additionally, existing studies concentrate on the stability of the intrinsic unstable perovskite for photocatalytic CO_2 reduction. It should be noted that if we can synthesize perovskite that is intrinsically stableagainst water, it is much better for photocatalytic CO_2 reduction, *e.g.*, $Cs_2Pt_xSn_{1-x}Cl_6$.[116]

Besides, low-dimensional halide perovskites allow great possibility for photocatalytic CO_2 reduction and solar fuel production.[117,118] In contrast with three-dimensional perovskite, two-dimensional (2D) perovskite generally has higher stability due to the hydrophobic bulky organic A-site cations in the structure.[119,120] Moreover, 2D perovskites have more surface defects because of their large specific area, rendering them good candidates for photocatalysis.[121] Li's group realized the stabilization of 2D hybrid perovskites in aqueous solution and found that the length of A-site organic cations could affect the nanostructures, electron transfer, and photocatalytic activity process significantly.[117]

Recently, thiocyanates (SCN^-) and formates ($HCOO^-$) have been utilized to synthesize stable pseudo-halide perovskite materials for application in solar cells.[122] Compared to halide perovskite, these pseudo-halide perovskites have better stability at room temperature because of the SCN^- or $HCOO^-$ anion in the axial positions of the lead halide octahedron which results in an asymmetric electronic structure to maintain the desired framework.[123] The tunable band structure and relatively low exciton binding energy of pseudo-halide perovskites also contribute to obtaining desirable bandgaps and electron transfer. From these perspectives, the pseudo-halide perovskite materials also show promising prospects for photocatalytic CO_2 reduction.

4.2 Pb-free perovskite

Due to the high toxicity of Pb, Pb-based perovskite would induce severe environmental pollution, which stops practical industrial application.[124,125] Unlike solar cells, whose toxicity could be mitigated by device encapsulation, a perovskite photocatalyst would directly come into contact with the surroundings. To solve this problem, some Pb-free perovskite QDs have been obtained, such as Cs_2SnI_6,[126,127] Cs_2AgBiX_6,[128] and $Cs_2NaBiCl_6$.[129] Nonetheless, the photocatalytic CO_2 activities of these
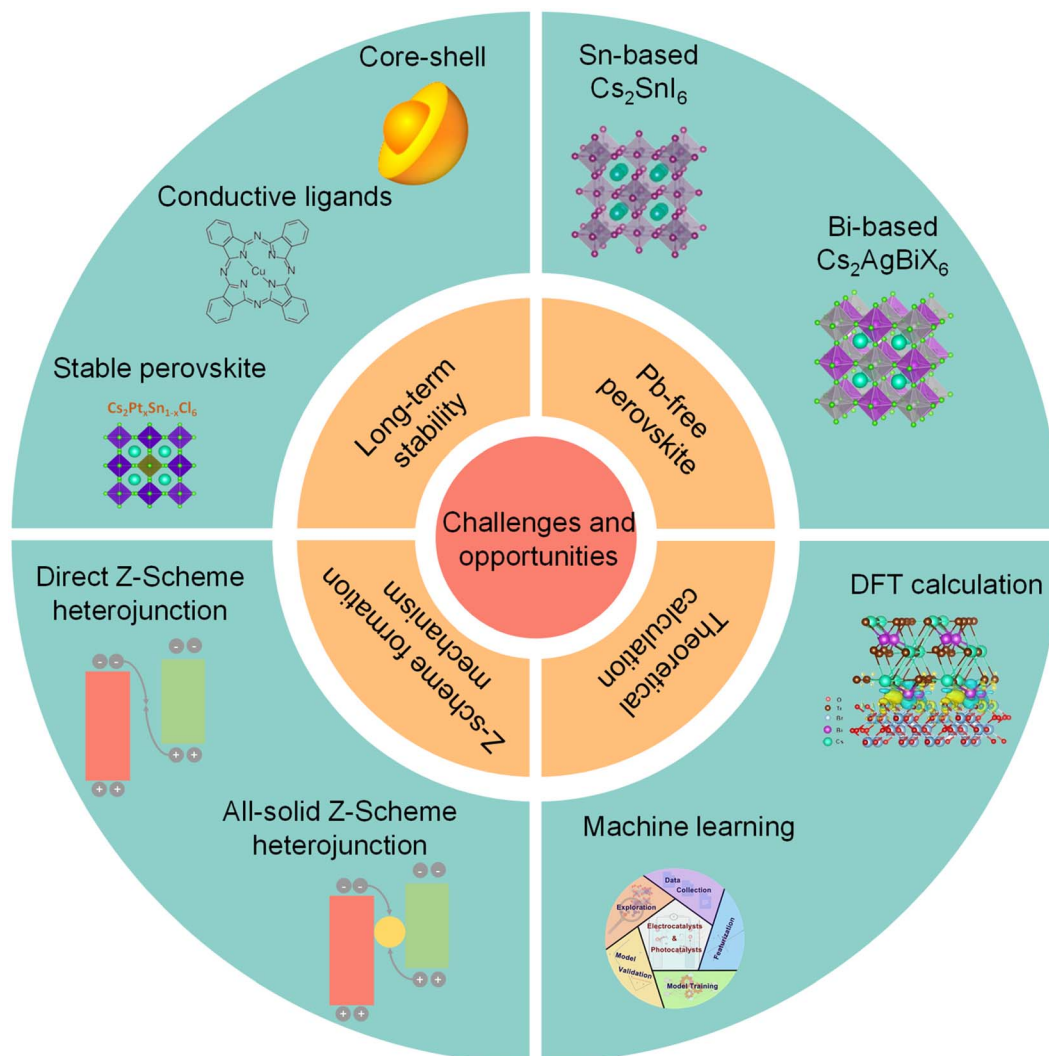
Fig. 11 Challenges and opportunities of photocatalytic CO_2 reduction on perovskite QDs. Insets are reproduced from ref. 35 with permission from Springer Nature, copyright 2018; reproduced from ref. 114 with permission from Springer Nature, copyright 2020; reproduced from ref. 116 with permission from Wiley–VCH, copyright 2021. Reproduced from ref. 127 with permission from Wiley–VCH, copyright 2021. Reproduced from ref. 128 with permission from American Chemical Society, copyright 2020. Reproduced from ref. 23 with permission from Wiley–VCH, copyright 2022. Reproduced from ref. 133 with permission from American Chemical Society, copyright 2022.

substitutions are lower than that of Pb-based perovskite QDs. As a result, much attention should be paid to finding stable low-toxic or non-toxic perovskite materials with high catalytic performance.[130]

4.3 Z-scheme formation mechanism

In the past few years, a *Z*-scheme heterojunction has acquired increasing interest because of higher redox potentials than the type-II heterojunction. So far, some studies have constructed perovskite-based *Z*-scheme heterojunctions.[23] Here are two questions to be addressed in the future. First, fabricating a *Z*-scheme heterojunction needs complicated conditions, including interfacial properties, surface ligands, band structures, and so on. To confirm whether a heterojunction corresponds to the *Z*-scheme, a series of advanced characterization studies should be carried out.[131] For example, *in situ* XPS can

demonstrate the changes in binding energy before and after light illumination. This can directly provide solid information to confirm the emergence of a *Z*-scheme heterojunction. Secondly, although an internal build-in electric field is a commonly used concept to explain the *Z*-scheme, the internal electric field also emerges in a type-II heterojunction. Therefore, the real formation mechanism of a *Z*-scheme heterojunction is still unclear for the whole catalysis field, and deserves more efforts from physicist, chemists, and materials scientists.[132]

4.4 Theoretical calculations and machine learning

DFT calculations can be used to understand the photocatalytic mechanism. For example, Lu, *et al.* conducted DFT to figure out the high selectivity of $Cs_3Bi_2Br_9$/mesoporous TiO_2 and Cs_2-$AgBiBr_6$/mesoporous TiO_2 for photocatalytic CO_2 reduction, and the results showed that the high selectivity was attributed to the

12494 | *J. Mater. Chem. A*, 2023, **11**, 12482–12498

This journal is © The Royal Society of Chemistry 2023

Bi-adsorption-mediated hydrogenation of CO (*HCO) rather than CO desorption.[23] Li's group used DFT to calculate the work function of $CsPbBr_3$ and $CsPbBr_3$ with Br vacancies to understand the different electron migration processes from $CsPbBr_3$ to g-C_3N_4.[27] Thus, DFT can provide valuable insights into the mechanism of photocatalytic CO_2 reduction and heterojunction construction. Besides, machine learning is a suite of data-driven computational methods that uses a range of algorithms to build models based on patterns in data, which can be applied to predict new structures and materials.[133] Recently, machine learning has been successfully utilized for the discovery and prediction of functional materials, such as electrocatalysts, photocatalysts, and optoelectronics.[134–136] For example, Chan *et al.* used machine learning and high-throughput computations to design mixed cation halide perovskite alloys.[137] Based on ABX_3 halide perovskite alloys where mixing occurs at the B-site, ~18 000 novel compounds were proposed and 392 were screened to be stable with suitable band gaps and defect tolerance. Hence, machine learning approaches can also be utilized to identify stable halide perovskite compositions and design new perovskite photocatalysts.

In conclusion, composition optimization, surface modification, and heterojunction construction are effective strategies to promote superior stability and efficient photocatalytic performance, which have been summarized in this review. However, it is still a challenge to realize long-term stability and high catalytic activity for perovskite-based photocatalysts. Construction of core–shell heterostructures and discovery of low-dimensional perovskite materials are promising approaches to overcome these obstacles. Besides, the photocatalytic CO_2 reduction path and *Z*-scheme formation mechanism should be further understood. DFT calculations, machine learning, and operando characterization can provide reliable and detailed information, which may help researchers understand these complicated processes.[137] Furthermore, to design and find low-lead or free-lead perovskite photocatalysts holds great promise for environment protection and practical applications. We hope that this review could provide some assistance for rational design of perovskite-based photocatalysts and attract more researchers to this promising research field.

Author contributions

W. S., G. Q, and B. L. conceived the idea and wrote the paper. B. L. supervised the project. All the authors contributed to the overall scientific interpretation and edited the manuscript.

Conflicts of interest

There are no conflicts to declare.

Acknowledgements

Notes and references

1 X. Gao and W. Yang, *Chem*, 2020, **6**, 1041–1042.

2 Y. Wang, E. Chen and J. Tang, *ACS Catal.*, 2022, **12**, 7300–7316.

3 G. Q. Zhao, J. Hu, X. Long, J. Zou, J. G. Yu and F. P. Jiao, *Small*, 2021, **17**, 2102155.

4 E. Gong, S. Ali, C. B. Hiragond, H. S. Kim, N. S. Powar, D. Kim, H. Kim and S.-I. In, *Energy Environ. Sci.*, 2022, **15**, 880–937.

5 Y. Wei, F. You, D. Zhao, J. Wan, L. Gu and D. Wang, *Angew. Chem., Int. Ed. Engl.*, 2022, **61**, e202212049.

6 X. Chen, S. Shen, L. Guo and S. S. Mao, *Chem. Rev.*, 2010, **110**, 6503–6570.

7 W. Song, Y. Wang, C. Wang, B. Wang, J. Feng, W. Luo, C. Wu, Y. Yao and Z. Zou, *ChemCatChem*, 2021, **13**, 1711–1716.

8 D. Li, K. Yang, J. Lian, J. Yan and S. Liu, *Adv. Energy Mater.*, 2022, **12**, 2201070.

9 A. Kojima, K. Teshima, Y. Shirai and T. Miyasaka, *J. Am. Chem. Soc.*, 2009, **131**, 6050–6051.

10 Y. Hou, E. Aydin, M. De Bastiani, C. Xiao, F. H. Isikgor, D. J. Xue, B. Chen, H. Chen, B. Bahrami, A. H. Chowdhury, A. Johnston, S. W. Baek, Z. Huang, M. Wei, Y. Dong, J. Troughton, R. Jalmood, A. J. Mirabelli, T. G. Allen, E. Van Kerschaver, M. I. Saidaminov, D. Baran, Q. Qiao, K. Zhu, S. De Wolf and E. H. Sargent, *Science*, 2020, **367**, 1135–1140.

11 J. Peng, F. Kremer, D. Walter, Y. Wu, Y. Ji, J. Xiang, W. Liu, T. Duong, H. Shen, T. Lu, F. Brink, D. Zhong, L. Li, O. Lee Cheong Lem, Y. Liu, K. J. Weber, T. P. White and K. R. Catchpole, *Nature*, 2022, **601**, 573–578.

12 G. Nedelcu, L. Protesescu, S. Yakunin, M. I. Bodnarchuk, M. J. Grotevent and M. V. Kovalenko, *Nano Lett.*, 2015, **15**, 5635–5640.

13 D. Ma, K. Lin, Y. Dong, H. Choubisa, A. H. Proppe, D. Wu, Y. K. Wang, B. Chen, P. Li, J. Z. Fan, F. Yuan, A. Johnston, Y. Liu, Y. Kang, Z. H. Lu, Z. Wei and E. H. Sargent, *Nature*, 2021, **599**, 594–598.

14 C. R. Kagan, E. Lifshitz, E. H. Sargent and D. V. Talapin, *Science*, 2016, **353**, aac5523.

15 K. Sakhatskyi and M. V. Kovalenko, *Light Sci. Appl.*, 2022, **11**, 271.

16 H. Tsai, S. Shrestha, R. A. Vilá, W. Huang, C. Liu, C.-H. Hou, H.-H. Huang, X. Wen, M. Li, G. Wiederrecht, Y. Cui, M. Cotlet, X. Zhang, X. Ma and W. Nie, *Nat. Photon.*, 2021, **15**, 843–849.

17 L. Protesescu, S. Yakunin, M. I. Bodnarchuk, F. Krieg, R. Caputo, C. H. Hendon, R. X. Yang, A. Walsh and M. V. Kovalenko, *Nano Lett.*, 2015, **15**, 3692–3696.

18 Y. F. Xu, M. Z. Yang, B. X. Chen, X. D. Wang, H. Y. Chen, D. B. Kuang and C. Y. Su, *J. Am. Chem. Soc.*, 2017, **139**, 5660–5663.

19 Y. Jiang, H. Y. Chen, J. Y. Li, J. F. Liao, H. H. Zhang, X. D. Wang and D. B. Kuang, *Adv. Funct. Mater.*, 2020, **30**, 2004293.

This journal is © The Royal Society of Chemistry 2023

J. Mater. Chem. A, 2023, **11**, 12482–12498 | **12495**

20 M. Ou, W. Tu, S. Yin, W. Xing, S. Wu, H. Wang, S. Wan, Q. Zhong and R. Xu, *Angew. Chem., Int. Ed. Engl.*, 2018, **130**, 13758–13762.

21 Z. J. Li, E. Hofman, J. Li, A. H. Davis, C. H. Tung, L. Z. Wu and W. Zheng, *Adv. Funct. Mater.*, 2017, **28**, 1704288.

22 H. Huang, D. Verhaeghe, B. Weng, B. Ghosh, H. Zhang, J. Hofkens, J. A. Steele and M. B. J. Roeffaers, *Angew. Chem., Int. Ed. Engl.*, 2022, **61**, e202203261.

23 Q. M. Sun, J. J. Xu, F. F. Tao, W. Ye, C. Zhou, J. H. He and J. M. Lu, *Angew. Chem., Int. Ed. Engl.*, 2022, **61**, e202200872.

24 J. Yuan, H. Liu, S. Wang and X. Li, *Nanoscale*, 2021, **13**, 10281–10304.

25 J. T. DuBose and P. V. Kamat, *ACS Energy Lett.*, 2022, **7**, 1994–2011.

26 J. Wang, Y. Shi, Y. Wang and Z. Li, *ACS Energy Lett.*, 2022, **7**, 2043–2059.

27 Q. Zheng, J. Wang, X. Li, Y. Bai, Y. Li, J. Wang, Y. Shi, X. Jiang and Z. Li, *ACS Mater. Lett.*, 2022, **4**, 1638–1645.

28 R. Das, A. Patra, S. K. Dutta, S. Shyamal and N. Pradhan, *J. Am. Chem. Soc.*, 2022, **144**, 18629–18641.

29 S. Chen, H. Yin, P. Liu, Y. Wang and H. Zhao, *Adv. Mater.*, 2022, 2203836.

30 X. Ling, J. Yuan and W. Ma, *Acc. Mater. Res.*, 2022, **3**, 866–878.

31 Y. Tang, S. Tang, M. Luo, Y. Guo, Y. Zheng, Y. Lou and Y. Zhao, *Chem. Commun.*, 2021, **57**, 7465–7479.

32 J. Y. Kim, J. W. Lee, H. S. Jung, H. Shin and N. G. Park, *Chem. Rev.*, 2020, **120**, 7867–7918.

33 J. A. Steele, H. Jin, I. Dovgaliuk, R. F. Berger, T. Braeckevelt, H. Yuan, C. Martin, E. Solano, K. Lejaeghere, S. M. J. Rogge, C. Notebaert, W. Vandezande, K. P. F. Janssen, B. Goderis, E. Debroye, Y. K. Wang, Y. Dong, D. Ma, M. Saidaminov, H. Tan, Z. Lu, V. Dyadkin, D. Chernyshov, V. Van Speybroeck, E. H. Sargent, J. Hofkens and M. B. J. Roeffaers, *Science*, 2019, **365**, 679–684.

34 R. X. Yang and L. Z. Tan, *J. Chem. Phys.*, 2020, **152**, 034702.

35 Q. A. Akkerman, G. Raino, M. V. Kovalenko and L. Manna, *Nat. Mater.*, 2018, **17**, 394–405.

36 E. M. Sanehira, A. R. Marshall, J. A. Christians, S. P. Harvey, P. N. Ciesielski, L. M. Wheeler, P. Schulz, L. Y. Lin, M. C. Beard and J. M. Luther, *Sci. Adv.*, 2017, **3**, eaao4204.

37 J. W. Lee, S. Tan, S. I. Seok, Y. Yang and N. G. Park, *Science*, 2022, **375**, eabj1186.

38 B. Chen, P. N. Rudd, S. Yang, Y. Yuan and J. Huang, *Chem. Soc. Rev.*, 2019, **48**, 3842–3867.

39 X. K. Liu, W. Xu, S. Bai, Y. Jin, J. Wang, R. H. Friend and F. Gao, *Nat. Mater.*, 2021, **20**, 10–21.

40 D. P. Nenon, K. Pressler, J. Kang, B. A. Koscher, J. H. Olshansky, W. T. Osowiecki, M. A. Koc, L. W. Wang and A. P. Alivisatos, *J. Am. Chem. Soc.*, 2018, **140**, 17760–17772.

41 D. Voiry, H. S. Shin, K. P. Loh and M. Chhowalla, *Nat. Rev. Chem.*, 2018, **2**, 17105.

42 S. Navarro-Jaén, M. Virginie, J. Bonin, M. Robert, R. Wojcieszak and A. Y. Khodakov, *Nat. Rev. Chem.*, 2021, **5**, 564–579.

43 Y. Ma, X. Wang, Y. Jia, X. Chen, H. Han and C. Li, *Chem. Rev.*, 2014, **114**, 9987–10043.

44 J. Gan, J. He, R. L. Z. Hoye, A. Mavlonov, F. Raziq, J. L. MacManus-Driscoll, X. Wu, S. Li, X. Zu, Y. Zhan, X. Zhang and L. Qiao, *ACS Energy Lett.*, 2019, **4**, 1308–1320.

45 H. Huang, B. Pradhan, J. Hofkens, M. B. J. Roeffaers and J. A. Steele, *ACS Energy Lett.*, 2020, **5**, 1107–1123.

46 F. Krieg, S. T. Ochsenbein, S. Yakunin, S. Ten Brinck, P. Aellen, A. Suess, B. Clerc, D. Guggisberg, O. Nazarenko, Y. Shynkarenko, S. Kumar, C. J. Shih, I. Infante and M. V. Kovalenko, *ACS Energy Lett.*, 2018, **3**, 641–646.

47 J. Shamsi, Z. Dang, P. Ijaz, A. L. Abdelhady, G. Bertoni, I. Moreels and L. Manna, *Chem. Mater.*, 2018, **30**, 79–83.

48 S. Park, W. J. Chang, C. W. Lee, S. Park, H.-Y. Ahn and K. T. Nam, *Nat. Energy*, 2016, **2**, 16185.

49 X. Zhang, R. Tang, F. Li, R. Zheng and J. Huang, *Sol. RRL*, 2022, **6**, 202101058.

50 J. A. Christians, P. A. Miranda Herrera and P. V. Kamat, *J. Am. Chem. Soc.*, 2015, **137**, 1530–1538.

51 M.-G. Ju, M. Chen, Y. Zhou, J. Dai, L. Ma, N. P. Padture and X. C. Zeng, *Joule*, 2018, **2**, 1231–1241.

52 Y. Zhou and Y. Zhao, *Energy Environ. Sci.*, 2019, **12**, 1495–1511.

53 N. Li, X. Chen, J. Wang, X. Liang, L. Ma, X. Jing, D. L. Chen and Z. Li, *ACS Nano*, 2022, **16**, 3332–3340.

54 A. Senocrate, T. Acartürk, G. Y. Kim, R. Merkle, U. Starke, M. Grätzel and J. Maier, *J. Mater. Chem. A*, 2018, **6**, 10847–10855.

55 J. Chen, X. Hong, Y. Wang, X. Guan, R. Wang, Y. Wang, H. Du, Y. Zhang and S. Shen, *J. Phys. Chem. Lett.*, 2022, **13**, 1806–1824.

56 W. Chi and S. K. Banerjee, *Chem. Mater.*, 2021, **33**, 4269–4303.

57 T. Zhang, M. I. Dar, G. Li, F. Xu, N. Guo, M. Gratzel and Y. Zhao, *Sci. Adv.*, 2017, **3**, e1700841.

58 Y. K. Wang, K. Singh, J. Y. Li, Y. Dong, X. Q. Wang, J. M. Pina, Y. J. Yu, R. Sabatini, Y. Liu, D. Ma, J. Liu, Z. Liu, Y. Gao, O. Voznyy, W. Ma, M. K. Fung, L. S. Liao and E. H. Sargent, *Adv. Mater.*, 2022, **34**, 2200854.

59 C. C. Lin, T. R. Liu, S. R. Lin, K. M. Boopathi, C. H. Chiang, W. Y. Tzeng, W. C. Chien, H. S. Hsu, C. W. Luo, H. Y. Tsai, H. A. Chen, P. C. Kuo, J. Shiue, J. W. Chiou, W. F. Pong, C. C. Chen and C. W. Chen, *J. Am. Chem. Soc.*, 2022, **144**, 15718–15726.

60 L. Li and Z. Zhang, *Chem. Eng. J.*, 2022, **434**, 134811.

61 C. Tang, C. Chen, W. Xu and L. Xu, *J. Mater. Chem. A*, 2019, **7**, 6911–6919.

62 C. H. Lu, G. V. Biesold-McGee, Y. Liu, Z. Kang and Z. Lin, *Chem. Soc. Rev.*, 2020, **49**, 4953–5007.

63 Y. Gao, Y. Cui, J. Li, Y. Xu, J. Hu and T. He, *J. Phys. Chem. C*, 2022, **126**, 6694–6699.

64 H. Bian, T. Liu, D. Li, Z. Xu, J. Lian, M. Chen, J. Yan and S. Frank Liu, *Chem. Eng. J.*, 2022, **435**, 135071.

65 Y. Guo, J. Su, L. Wang, Z. Lin, Y. Hao and J. Chang, *J. Phys. Chem. Lett.*, 2021, **12**, 3393–3400.

66 J. Zhu, L. Zhou, Y. Zhu, J. Huang, L. Hou, J. Shen, S. Dai and C. Li, *Small*, 2022, **18**, 2104399.

12496 | *J. Mater. Chem. A*, 2023, **11**, 12482–12498

This journal is © The Royal Society of Chemistry 2023

67 M. T. Hoang, A. S. Pannu, C. Tang, Y. Yang, N. D. Pham, K. Gui, X. Wang, S. Yambem, P. Sonar, A. Du and H. Wang, *Adv. Opt. Mater.*, 2020, **8**, 202000742.

68 D. H. Parmar, J. M. Pina, H. Choubisa, G. Bappi, K. Bertens and E. H. Sargent, *Adv. Mater.*, 2021, **33**, 2008690.

69 J. Li, X. Du, G. Niu, H. Xie, Y. Chen, Y. Yuan, Y. Gao, H. Xiao, J. Tang, A. Pan and B. Yang, *ACS Appl. Mater. Interfaces*, 2020, **12**, 989–996.

70 P. Li, Y. Lin, M. Ma, M. Zhang, J. Li, Z. Wang, V. Maheskumar, Z.-Y. Jiang and R. Zhang, *ACS Appl. Energy Mater.*, 2022, **5**, 1942–1952.

71 Y.-X. Feng, G.-X. Dong, K. Su, Z.-L. Liu, W. Zhang, M. Zhang and T.-B. Lu, *J. Energy Chem.*, 2022, **69**, 348–355.

72 N. H. Alotaibi, G. M. Mustafa, N. A. Kattan, Q. Mahmood, H. Albalawi, M. Morsi, H. H. Somaily, M. A. Hafez, H. I. Mahmoud and M. A. Amin, *J. Solid State Chem.*, 2022, **313**, 123353.

73 Z. Liu, H. Yang, J. Wang, Y. Yuan, K. Hills-Kimball, T. Cai, P. Wang, A. Tang and O. Chen, *Nano Lett.*, 2021, **21**, 1620–1627.

74 S.-H. Guo, J. Zhou, X. Zhao, C.-Y. Sun, S.-Q. You, X.-L. Wang and Z.-M. Su, *J. Catal.*, 2019, **369**, 201–208.

75 L. Chouhan, S. Ghimire, C. Subrahmanyam, T. Miyasaka and V. Biju, *Chem. Soc. Rev.*, 2020, **49**, 2869–2885.

76 J. Hou, S. Cao, Y. Wu, Z. Gao, F. Liang, Y. Sun, Z. Lin and L. Sun, *Eur. J. Chem.*, 2017, **23**, 9481–9485.

77 S. Shyamal, S. K. Dutta, T. Das, S. Sen, S. Chakraborty and N. Pradhan, *J. Phys. Chem. Lett.*, 2020, **11**, 3608–3614.

78 Q. A. Akkerman, T. P. T. Nguyen, S. C. Boehme, F. Montanarella, D. N. Dirin, P. Wechsler, F. Beiglböck, G. Raino, R. Erni, C. Katan, J. Even and M. V. Kovalenko, *Science*, 2022, **377**, 1406–1412.

79 W. Fu, A. G. Ricciardulli, Q. A. Akkerman, R. A. John, M. M. Tavakoli, S. Essig, M. V. Kovalenko and M. Saliba, *Mater. Today*, 2022, **58**, 275–296.

80 S. Tan, T. Huang, I. Yavuz, R. Wang, M. H. Weber, Y. Zhao, M. Abdelsamie, M. E. Liao, H. C. Wang, K. Huynh, K. H. Wei, J. Xue, F. Babbe, M. S. Goorsky, J. W. Lee, C. M. Sutter-Fella and Y. Yang, *J. Am. Chem. Soc.*, 2021, **143**, 6781–6786.

81 Y. F. Lan, J. S. Yao, J. N. Yang, Y. H. Song, X. C. Ru, Q. Zhang, L. Z. Feng, T. Chen, K. H. Song and H. B. Yao, *Nano Lett.*, 2021, **21**, 8756–8763.

82 Y. Bai, M. Hao, S. Ding, P. Chen and L. Wang, *Adv. Mater.*, 2022, **34**, 2105958.

83 J. Xue, R. Wang and Y. Yang, *Nat. Rev. Mater.*, 2020, **5**, 809–827.

84 S. Liang, S. He, M. Zhang, Y. Yan, T. Jin, T. Lian and Z. Lin, *J. Am. Chem. Soc.*, 2022, **144**, 12901–12914.

85 J.-C. Wang, N. Li, A. M. Idris, J. Wang, X. Du, Z. Pan and Z. Li, *Sol. RRL*, 2021, **5**, 202100154.

86 W. Song, D. Wang, J. Tian, G. Qi, M. Wu, S. Liu, T. Wang, B. Wang, Y. Yao, Z. Zou and B. Liu, *Small*, 2022, **18**, 2204763.

87 S. Purohit, S. Shyamal, S. K. Saini, K. L. Yadav, M. Kumar and S. Satapathi, *Energy Fuels*, 2022, **36**, 12170–12180.

88 H. Xiao, J. Fu, X. Wei, B. Wang, Q. Qian, J. Huang, R. Li and Z. Zang, *Laser Photonics Rev.*, 2022, **16**, 2200276.

89 Y. Jiang, J.-F. Liao, Y.-F. Xu, H.-Y. Chen, X.-D. Wang and D.-B. Kuang, *J. Mater. Chem. A*, 2019, **7**, 13762–13769.

90 Q. J. Wu, J. Liang, Y. B. Huang and R. Cao, *Acc. Chem. Res.*, 2022, **55**, 2978–2997.

91 C. Zhang, W. Li and L. Li, *Angew. Chem., Int. Ed.*, 2021, **60**, 7488–7501.

92 Z.-C. Kong, J.-F. Liao, Y.-J. Dong, Y.-F. Xu, H.-Y. Chen, D.-B. Kuang and C.-Y. Su, *ACS Energy Lett.*, 2018, **3**, 2656–2662.

93 Z. Zhang, B. Wang, H.-B. Zhao, J.-F. Liao, Z.-C. Zhou, T. Liu, B. He, Q. Wei, S. Chen, H.-Y. Chen, D.-B. Kuang, Y. Li and G. Xing, *Appl. Catal., B*, 2022, **312**, 121358.

94 Y.-H. Chen, J.-K. Ye, Y.-J. Chang, T.-W. Liu, Y.-H. Chuang, W.-R. Liu, S.-H. Liu and Y.-C. Pu, *Appl. Catal., B*, 2021, **284**, 119751.

95 Y. Tang, C. H. Mak, G. Jia, K.-C. Cheng, J.-J. Kai, C.-W. Hsieh, F. Meng, W. Niu, F.-F. Li, H.-H. Shen, X. Zhu, H. M. Chen and H.-Y. Hsu, *J. Mater. Chem. A*, 2022, **10**, 12296–12316.

96 R. Tang, H. Sun, Z. Zhang, L. Liu, F. Meng, X. Zhang, W. Yang, Z. Li, Z. Zhao, R. Zheng and J. Huang, *Chem. Eng. J.*, 2022, **429**, 132137.

97 J.-N. Huang, Y.-J. Dong, H.-B. Zhao, H.-Y. Chen, D.-B. Kuang and C.-Y. Su, *J. Mater. Chem. A*, 2022, **10**, 25212–25219.

98 Y.-F. Xu, M.-Z. Yang, H.-Y. Chen, J.-F. Liao, X.-D. Wang and D.-B. Kuang, *ACS Appl. Energy Mater.*, 2018, **1**, 5083–5089.

99 T. Chen, M. Zhou, W. Chen, Y. Zhang, S. Ou and Y. Liu, *Sustain. Energy Fuels*, 2021, **5**, 3598–3605.

100 X. Huang, H. Li, C. Zhang, S. Tan, Z. Chen, L. Chen, Z. Lu, X. Wang and M. Xiao, *Nat. Commun.*, 2019, **10**, 1163.

101 J.-F. Liao, Y.-T. Cai, J.-Y. Li, Y. Jiang, X.-D. Wang, H.-Y. Chen and D.-B. Kuang, *J. Energy Chem.*, 2021, **53**, 309–315.

102 J. Chakkamalayath, G. V. Hartland and P. V. Kamat, *J. Phys. Chem. C*, 2021, **125**, 17881–17889.

103 S. R. Xu, J. L. Li, Q. L. Mo, K. Wang, G. Wu, Y. Xiao, X. Z. Ge and F. X. Xiao, *Inorg. Chem.*, 2022, **61**, 17828–17837.

104 S. Schunemann, M. van Gastel and H. Tuysuz, *ChemSusChem*, 2018, **11**, 2057–2061.

105 G. Yin, X. Qi, Y. Chen, Q. Peng, X. Jiang, Q. Wang, W. Zhang and X. Gong, *J. Mater. Chem. A*, 2022, **10**, 22468–22476.

106 X. D. Wang, Y. H. Huang, J. F. Liao, Y. Jiang, L. Zhou, X. Y. Zhang, H. Y. Chen and D. B. Kuang, *J. Am. Chem. Soc.*, 2019, **141**, 13434–13441.

107 R. Zhang, L. Li, Y. Li, D. Wang, Y. Lin and T. Xie, *Sol. RRL*, 2022, **6**, 2200536.

108 A. Mahmoud Idris, S. Zheng, L. Wu, S. Zhou, H. Lin, Z. Chen, L. Xu, J. Wang and Z. Li, *Chem. Eng. J.*, 2022, **446**, 137197.

109 L. Wu, S. Zheng, H. Lin, S. Zhou, A. Mahmoud Idris, J. Wang, S. Li and Z. Li, *J. Colloid Interface Sci.*, 2023, **629**, 233–242.

110 Y. Jiang, J.-F. Liao, H.-Y. Chen, H.-H. Zhang, J.-Y. Li, X.-D. Wang and D.-B. Kuang, *Chem*, 2020, **6**, 766–780.

111 K. Sakhatskyi, R. A. John, A. Guerrero, S. Tsarev, S. Sabisch, T. Das, G. J. Matt, S. Yakunin, I. Cherniukh, M. Kotyrba,

This journal is © The Royal Society of Chemistry 2023

J. Mater. Chem. A, 2023, **11**, 12482–12498 | **12497**

Y. Berezovska, M. I. Bodnarchuk, S. Chakraborty, J. Bisquert and M. V. Kovalenko, *ACS Energy Lett.*, 2022, **7**, 3401–3414.

112 J. Ma, M. Qin, P. Li, L. Han, Y. Zhang and Y. Song, *Energy Environ. Sci.*, 2022, **15**, 413–438.

113 C. Fu, Z. Gu, Y. Tang, Q. Xiao, S. Zhang, Y. Zhang and Y. Song, *Angew. Chem., Int. Ed.*, 2022, **61**, e202117067.

114 S. Fratini, M. Nikolka, A. Salleo, G. Schweicher and H. Sirringhaus, *Nat. Mater.*, 2020, **19**, 491–502.

115 L. Meng, C. Sun, R. Wang, W. Huang, Z. Zhao, P. Sun, T. Huang, J. Xue, J. W. Lee, C. Zhu, Y. Huang, Y. Li and Y. Yang, *J. Am. Chem. Soc.*, 2018, **140**, 17255–17262.

116 H. Yin, J. Chen, P. Guan, D. Zheng, Q. Kong, S. Yang, P. Zhou, B. Yang, T. Pullerits and K. Han, *Angew. Chem., Int. Ed.*, 2021, **60**, 22693–22699.

117 H. Wang, H. Zhang, J. Wang, Y. Gao, F. Fan, K. Wu, X. Zong and C. Li, *Angew. Chem., Int. Ed.*, 2021, **60**, 7376–7381.

118 L. Yan, J. Ma, P. Li, S. Zang, L. Han, Y. Zhang and Y. Song, *Adv. Mater.*, 2022, **34**, 2106822.

119 S. Peng, J. Ma, P. Li, S. Zang, Y. Zhang and Y. Song, *Adv. Funct. Mater.*, 2022, **32**, 2205289.

120 Q. Cao, P. Li, W. Chen, S. Zang, L. Han, Y. Zhang and Y. Song, *Nano Today*, 2022, **43**, 101394.

121 M. Que, W. Cai, Y. Zhao, Y. Yang, B. Zhang, S. Yun, J. Chen and G. Zhu, *J. Colloid Interface Sci.*, 2022, **610**, 538–545.

122 P. Y. Lin, A. Loganathan, I. Raifuku, M. H. Li, Y. Y. Chiu, S. T. Chang, A. Fakharuddin, C. F. Lin, T. F. Guo, L. Schmidt-Mende and P. Chen, *Adv. Energy Mater.*, 2021, **11**, 2100818.

123 C. H. Liao, C. H. Chen, J. Bing, C. Bailey, Y. T. Lin, T. M. Pandit, L. Granados, J. Zheng, S. Tang, B. H. Lin, H. W. Yen, D. R. McCamey, B. J. Kennedy, C. C. Chueh and A. W. Y. Ho-Baillie, *Adv. Mater.*, 2022, **34**, 2104782.

124 H. Zhu, J. Ma, P. Li, S. Zang, Y. Zhang and Y. Song, *Chem*, 2022, **8**, 2939–2960.

125 H. Luo, P. Li, J. Ma, L. Han, Y. Zhang and Y. Song, *Adv. Energy Mater.*, 2022, **12**, 2201242.

126 P. Zhou, H. Chen, Y. Chao, Q. Zhang, W. Zhang, F. Lv, L. Gu, Q. Zhao, N. Wang, J. Wang and S. Guo, *Nat. Commun.*, 2021, **12**, 4412.

127 S. Ullah, J. Wang, P. Yang, L. Liu, J. khan, S.-E. Yang, T. Xia, H. Guo and Y. Chen, *Sol. RRL*, 2021, **5**, 2000830.

128 D. J. Kubicki, M. Saski, S. MacPherson, K. Gal Kowski, J. Lewinski, D. Prochowicz, J. J. Titman and S. D. Stranks, *Chem. Mater.*, 2020, **32**, 8129–8138.

129 J. Pi, X. Jia, Z. Long, S. Yang, H. Wu, D. Zhou, Q. Wang, H. Zheng, Y. Yang, J. Zhang and J. Qiu, *Adv. Energy Mater.*, 2022, **12**, 2202074.

130 S. Bera, A. Patra, S. Shyamal, D. Nasipuri and N. Pradhan, *ACS Energy Lett.*, 2022, **7**, 3015–3023.

131 Y. Wang, X. Shang, J. Shen, Z. Zhang, D. Wang, J. Lin, J. C. S. Wu, X. Fu, X. Wang and C. Li, *Nat. Commun.*, 2020, **11**, 3043.

132 E. M. Akinoglu, D. A. Hoogeveen, C. Cao, A. N. Simonov and J. J. Jasieniak, *ACS Nano*, 2021, **15**, 7860–7878.

133 H. Mai, T. C. Le, D. Chen, D. A. Winkler and R. A. Caruso, *Chem. Rev.*, 2022, **122**, 13478–13515.

134 R. Gomez-Bombarelli, J. Aguilera-Iparraguirre, T. D. Hirzel, D. Duvenaud, D. Maclaurin, M. A. Blood-Forsythe, H. S. Chae, M. Einzinger, D. G. Ha, T. Wu, G. Markopoulos, S. Jeon, H. Kang, H. Miyazaki, M. Numata, S. Kim, W. Huang, S. I. Hong, M. Baldo, R. P. Adams and A. Aspuru-Guzik, *Nat. Mater.*, 2016, **15**, 1120–1127.

135 K. T. Butler, D. W. Davies, H. Cartwright, O. Isayev and A. Walsh, *Nature*, 2018, **559**, 547–555.

136 S. Chmiela, H. E. Sauceda, K. R. Muller and A. Tkatchenko, *Nat. Commun.*, 2018, **9**, 3887.

137 A. Mannodi-Kanakkithodi and M. K. Y. Chan, *Energy Environ. Sci.*, 2022, **15**, 1930–1949.

12498 | *J. Mater. Chem. A*, 2023, **11**, 12482–12498

This journal is © The Royal Society of Chemistry 2023